Evolution of a Dark Vortex on Neptune with Transient Secondary Features

Michael H. Wong <mikewong@astro.berkeley.edu>
Center for Integrative Planetary Science,
University of California, Berkeley CA 94720-3411, USA

Lawrence Sromovsky and Patrick Fry
University of Wisconsin, Madison WI, USA

Agustín Sánchez-Lavega, Ricardo Hueso, and Jon Legarreta
Universidad del País Vasco, Bilbao, Spain

Amy A. Simon
NASA Goddard Space Flight Center, Greenbelt MD, USA

Raúl Morales-Juberías
New Mexico Institute of Technology, Soccoro NM, USA

Joshua Tollefson and Imke de Pater
Departments of Astronomy and of Earth and Planetary Science, University of California, Berkeley CA 94720, USA

Patrick G.J. Irwin
Department of Physics, University of Oxford, Oxford, UK

Abstract:
Dark spots on Neptune observed by Voyager and the Hubble Space Telescope are thought to be anticyclones with lifetimes of a few years, in contrast with very long-lived anticyclones in Jupiter and Saturn. The full life cycle of any Neptune dark spot has not been captured due to limited temporal coverage, but our Hubble observations of a recent feature, NDS-2018, provide the most complete long-term observational history of any dark vortex on Neptune. Past observations suggest some dark spots meet their demise by fading and dissipating without migrating meridionally. On the other hand, simulations predict a second pathway with equatorward migration and disruption. Our HST observations suggest NDS-2018 is following the second pathway.

Some of the HST observations reveal transient dark features with widths of about 4000 to 9000 km, at latitudes between NDS-2018 and the equator. The secondary dark features appeared before changes in the meridional migration of NDS-2018 were seen. These features have somewhat smaller size and much smaller contrast compared to the main dark spot. Discrete secondary dark features of this scale have never been seen near previous dark spots, but global-scale dark bands are associated with several previous dark spots in addition to NDS-2018. The absolute photometric contrast of NDS-2018 (as large as 19%) is greater than previous dark spots, including the Great Dark Spot seen by Voyager. New simulations suggest that vortex internal circulation is weak relative to the background vorticity, presenting a clearly different case from stronger anticyclones observed on Jupiter and Saturn.

1. Introduction and background

The recent discovery of NDS-2018 (Simon et al., 2019) and subsequent observations of its behavior provide a new opportunity to understand the dynamics of dark vortices on Neptune. Although winds within dark spots on Neptune have never been directly tracked, only anticyclones should be stable within the observed anticyclonic shear environment at low latitudes (Sromovsky et al., 1993; Marcus, 1990). The Great Dark Spot (GDS) observed by Voyager 2 gave a visual impression of anticyclonic rotation (Smith et al., 1989), and numerical models (Polvani et al., 1990) supported the anticyclonic vortex interpretation by matching the measured dark spot bulk motions. Overall atmospheric dynamics on Neptune have been constrained by detailed measurements of winds, based on tracking of CH_4-ice clouds in time-series imaging (e.g., Limaye and Sromovsky, 1991; Karkoschka 2011; Fitzpatrick et al., 2014; Tollefson et al., 2018; Sánchez-Lavega et al., 2019). At deeper levels below the CH_4-ice clouds, dynamics are more difficult to constrain, and dark vortices, which are assumed to be located at deeper levels than the upper clouds (Smith et al., 1989; Limaye and Sromovsky, 1991; Irwin et al., 2022), have the potential to constrain parameters such as the deep thermal structure and wind field.

The Voyager 2 imaging dataset was unique in its frequent temporal sampling over a period of almost three months, allowing shape and positional oscillations to be measured for both the GDS and the smaller Dark Spot 2, or DS2 (Hammel et al., 1989; Sromovsky et al., 1993). The shape oscillations matched analytical predictions (Polvani et al., 1990) from the Kida equations (Kida, 1981), and oscillations continue to be used as key constraints for numerical models in the present day (Hadland et al., 2020). The LeBeau and Dowling (1998) numerical model predicted that the southern-hemisphere GDS observed by Voyager should migrate northward toward the equator, eventually disrupting at a critical latitude of about 15° S.

The fate of GDS was not observed within Voyager's limited observational time coverage; both GDS and DS2 were already fully formed when Voyager arrived at Neptune and survived throughout the four-month long Voyager encounter (Sromovsky et al., 1993). Hubble Space Telescope (HST) observations in October 1991 showed no signs of clouds between 40° S and the equator with brightness comparable to that of the GDS companion clouds (Sromovsky et al., 1995). However, HST could not directly resolve dark spots until the installation of corrective optics, at which point observations in October and November of 1994 confirmed that the GDS was gone (Hammel et al., 1995). Hubble data revealed several dark spots since then (Hammel et al., 1995; Sromovsky et al., 2001; Wong et al., 2018), but none were as large as the GDS until the discovery of NDS-2018, which gives a first chance to observe the long-term motions and potentially the demise of a GDS-scale dark spot. The timing of the origin and evolution of NDS-2018 are better established than for Neptune's past vortices, thanks to the annual cadence of the Outer Planet Atmospheres Legacy (OPAL) program (Simon et al., 2015).

2. Observations

HST is currently the only facility capable of detecting dark spots on Neptune. Observations using its Wide Field Camera 3 (WFC3; Dressel, 2021) were acquired and processed as described in Appendix A. To show non-global features, we used a "difference image" technique to subtract a smooth background (Sromovsky et al., 2001). Figure 1 illustrates this process for the last epoch out of the seven listed in Table 1. The resulting global maps (Fig. 2) show NDS-2018 as a prominent feature, along with other discrete features: nearby bright companion clouds near the time of formation in 2018, and a secondary dark feature at four epochs in 2019 and 2020. Although it is possible that the secondary dark feature(s) was related to the evolution of the NDS-2018, this conjecture cannot be proven with the available data, and in fact it is uncertain whether the secondary dark feature(s) are a single feature or separate transient features.
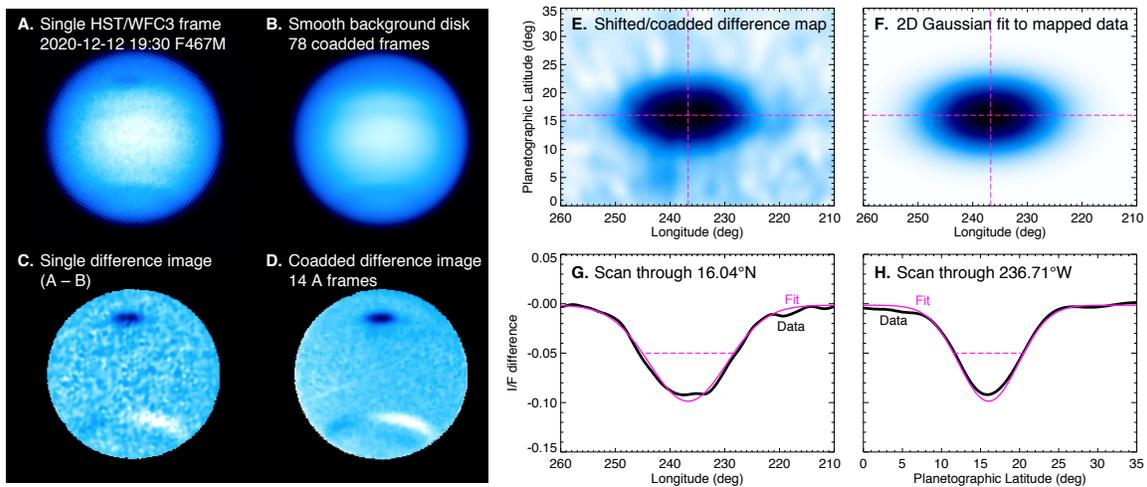

Fig. 1. Image processing and analysis. Dark spot morphology (size, position, shape) and contrast are measured using a uniform process with photometric cuts through maps at each epoch, corrected for limb-darkening. Data from December 2020 are used here to demonstrate the process. **(a)** A single image shows the dark spot, with limb darkening and pixel-to-pixel noise. **(b)** A stack of 78 coadded frames gives a background image with a high signal-to-noise ratio. **(c)** Meridional gradients and limb darkening are removed in the A – B difference image. **(d)** Signal-to-noise level is improved by stacking 14 frames showing the dark spot (corrected for planetary rotation and re-projected onto the disk for comparison). **(e)** The rectangularly-gridded version of difference image D is used as the basis for measuring photometric and morphological properties of the dark spot. Dashed lines show the fitted center latitude and longitude locations. **(f)** We perform a 2D Gaussian fit to the data in map E. **(g)** An east-west photometric cut through the dark spot at the latitude of the fitted Gaussian center compares the fitted profile with the observations. The east-west width is defined as the full width at half maximum of the Gaussian fit (dashed line). In the east-west direction, the vortex profile has a "flat bottom," such that the Gaussian fit slightly overestimates the maximum contrast of the feature. **(h)** Due to the size and shape of the dark spot, no flat bottom is observed in a north-south photometric cut through the center of the feature.

Table 1. HST/WFC3 observations of NDS-2018 on Neptune.

Times (UTC)	Program ID	Filters	Number of frames (F467M)		Secondary dark features
			NDS-2018	Background	
2018.70 (2018-09-10 01:58 to 2018-09-10 02:36)	OPAL GO-15262 (PI Simon)	F467M, F547M, F657N, F763M, F845M, FQ619N, FQ727N	2	9	–
2018.85 (2018-11-05 13:30 to 2018-11-06 09:13)	OPAL GO-15262 (PI Simon)	F467M, F547M, F657N, F763M, F845M, FQ619N, FQ727N	4	12	–
2019.75 (2019-09-28 16:56 to 2019-09-29 12:39)	OPAL GO-15502 (PI Simon)	F467M, F547M, F657N, F763M, F845M, FQ619N, FQ727N	4	14	4
2020.02 (2020-01-07 22:22 to 2020-01-07 23:06)	DDT GO-16057 (PI Wong)	F467M, F547M, F763M, F845M, FQ619N	8	24	8
2020.49 (2020-06-28 22:22 to 2020-06-28 23:06)	Midcycle GO-16084 (PI Wong)	F467M, F547M, F763M, F845M, FQ619N	8	32	8
2020.64 (2020-08-20 05:14 to 2020-08-20 05:52)	OPAL GO-15929 (PI Simon)	F467M, F547M, F657N, F763M, F845M, FQ619N, FQ727N	4	10	4
2020.95 (2020-12-12 19:26 to 2020-12-13 15:13)	Midcycle GO-16454 (PI Wong)	F390M, F467M, F547M, F845M	28	78	–

Times listed in first column correspond to images showing NDS-2018.

Frame counts correspond to one or two Neptune rotations, depending on coverage at each epoch. Background frame counts refer to coadded data used for NDS-2018 background subtraction; background frame counts for secondary dark spots may vary slightly from this number.
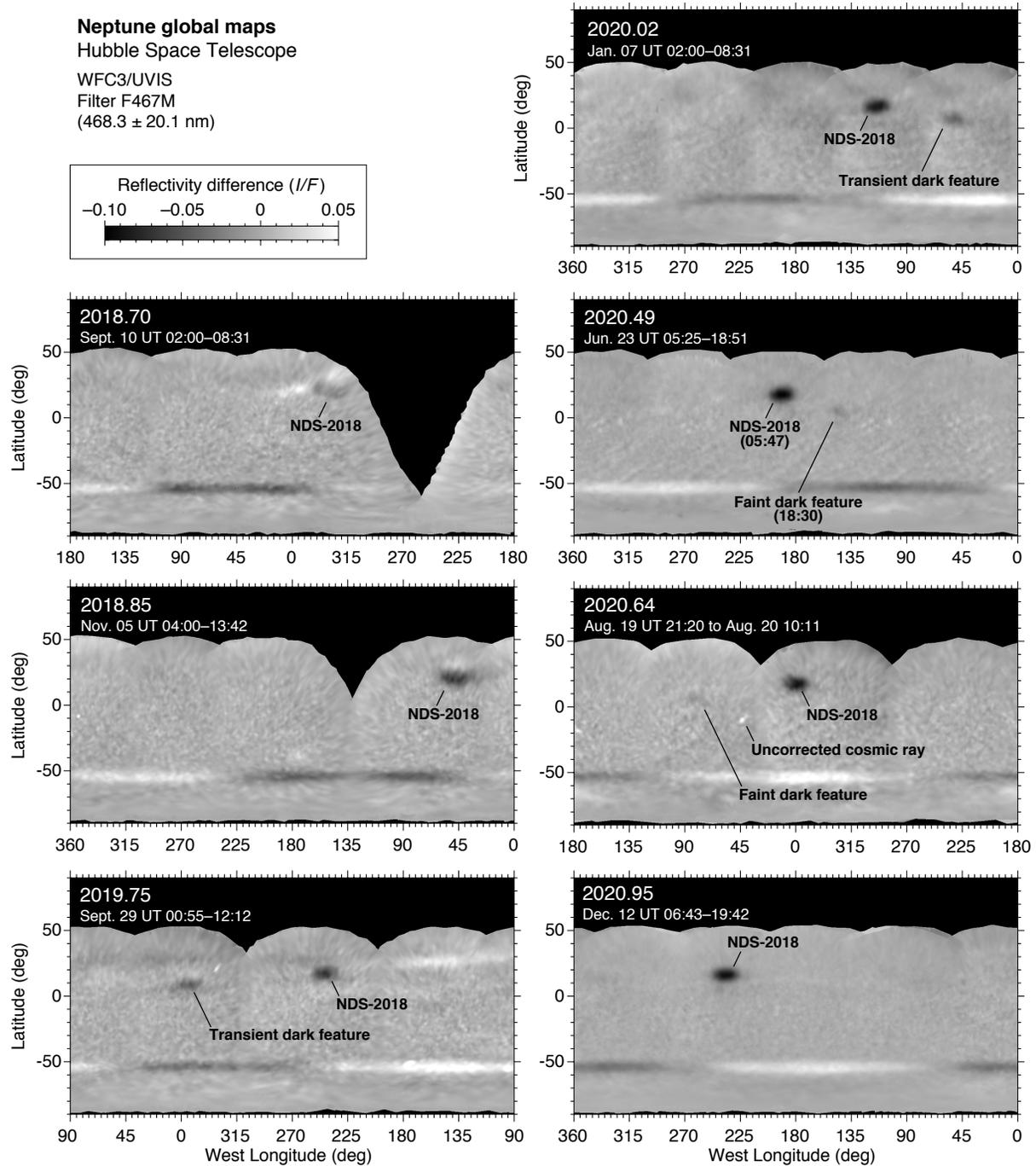
Neptune global maps
Hubble Space Telescope

WFC3/UVIS
Filter F467M
(468.3 ± 20.1 nm)

Reflectivity difference (*I/F*)

−0.10   −0.05   0   0.05

Fig. 2. Enhanced Neptune global maps over the 2018–2020 period. Difference maps show local reflectivity anomalies with respect to the longitudinal average. Companion clouds seen in 2018 were not seen in 2019 or 2020, and the contrast of the dark spot intensified as it drifted equatorward. Faint transient dark features are seen on the equatorward side of NDS-2018 in most epochs. At several epochs, the shape of NDS-2018 suggests a major axis that is inclined from an east-west orientation.

The secondary dark feature held a largely elliptical shape in September 2019 and January 2020, but the shape grew less defined in the June 2020 and August 2020 as the feature became smaller (Tables 2 and S1), and contrast was lower (Table 3). There is no feature of equivalent size in the December 2020 observations, although the existence of a very small dark feature immediately to the south of NDS-2018 cannot be ruled out. The central latitude of the transient dark feature(s), measured by 2D Gaussian fits in 2019 and January 2020, and by eye in June/August 2020, is shown as a function of time in Fig. 3b and listed in Table 4.
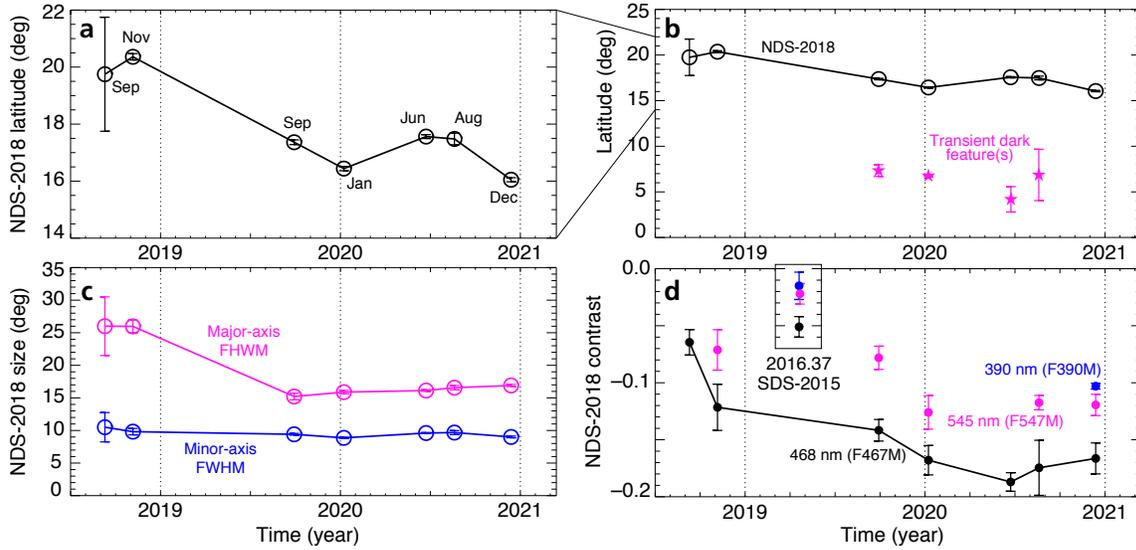

Fig. 3. Evolution of dark spot properties. (a) Despite a consistent equatorward drift from Sept. 2018 to Jan. 2020, NDS-2018 never drifted farther south than 16° N (planetographic latitudes are used throughout this paper). **(b)** Transient dark features developed prior to changes in drift of NDS-2018. The equatorward drift may have resumed in Dec. 2020 after transient dark features had vanished. **(c)** Width measurements show an initial shrinkage and circularization from 2018–2019, during the same period of rapid equatorward drift. The size/shape in 2019–2020 was roughly constant, with an aspect ratio of 1.74 ± 0.04. **(d)** Contrast for the previous dark spot (SDS-2015) is shown as an inset using the same *y*-axis scale. The measurement of the lowest contrast for NDS-2018, in Sept. 2018, may have been influenced by companion clouds overlying part of the dark spot (see Fig. 2).

Table 2. Transient secondary dark feature size and longitude offset.

Epoch	Secondary feature east-west width (km)		Secondary feature north-south width (km)		Longitude offset from NDS-2018 (deg)
2019.74	8815	± 3015	3368	± 3681	110
2020.02	7248	± 548	3358	± 209	–64
2020.48	3927	± 251	3224	± 109	–46
2020.63	5374	± 1142	3920	± 798	24

Table 3. NDS-2018 and secondary feature contrasts.

Epoch	NDS-2018 contrast (F467M)		NDS-2018 contrast (F547M)		NDS-2018 contrast (F390M)		Secondary feature contrast (F467M)	
2018.69	-0.065	± 0.011	–		–		–	
2018.85	-0.122	± 0.020	-0.071	± 0.018	–		–	
2019.74	-0.142	± 0.009	-0.078	± 0.010	–		-0.041	± 0.008
2020.02	-0.168	± 0.013	-0.126	± 0.015	–		-0.040	± 0.003
2020.48	-0.187	± 0.008	–		–		-0.015	± 0.011
2020.63	-0.175	± 0.024	-0.117	± 0.006	–		-0.018	± 0.007
2020.95	-0.166	± 0.014	-0.119	± 0.009	-0.103	± 0.003	–	

Table 4. NDS-2018 and secondary feature positions and drifts.

Epoch	NDS-2018 latitude		Secondary feature latitude		NDS-2018 longitude drift (m s⁻¹)		Tracking duration (hr)
2018.69	19.75	± 2.00	–		–		–
2018.85	20.36	± 0.11	–		288.7	± 4.2	19.15
2019.74	17.36	± 0.08	7.33	± 0.65	332.9	± 2.7	19.22
2020.02	16.44	± 0.08	6.76	± 0.09	333.5	± 72.8	0.72
2020.48	17.56	± 0.07	4.19	± 1.39	319.6	± 34.8	0.72
2020.63	17.48	± 0.20	6.86	± 2.82	328.6	± 5.7	16.04
2020.95	16.05	± 0.07	–		346.7	± 0.7	19.79

To quantify the photometric and morphological evolution of NDS-2018, we measured properties by fitting two-dimensional Gaussian profiles to the difference maps (Appendix B and Fig. 1). Over the period from discovery in September 2018 to January 2020, the dark spot maintained a roughly constant equatorward migration of 3.34°/year (Fig. 3). Continued migration at a constant rate should have brought the vortex to the critical latitude for disruption of 15° by June 2020, but the vortex reversed its equatorward drift in early 2020; it later resumed its equatorward migration in late 2020. Temporal sampling in the dataset is not fine enough to distinguish between a smooth drift with two latitude reversals, or a scenario including periodic latitudinal oscillations. All the measured latitudes in 2019 and 2020 fall within a range of 16.05° to 17.56°, a range that is only 1/3 the amplitude of the oscillations of DS2 (Sromovsky et al., 1993), and within the range of latitudinal oscillation amplitudes seen in numerical models (Hadland et al., 2020).

The vortex was largest when first observed in 2018, losing over 40% of its area by late 2019 when secondary dark features became visible (Fig. 2 and Table 5). The observations thus cannot rule out an origin of the transient dark features as fragments of the main anticyclone, perhaps similar to the "beads" seen by Voyager as they drifted away from the GDS (Fig. 4B of Smith et al., 1989; Fig. 1b of Sromovsky et al., 1993). The shrinking of NDS-2018 is quite different from the behavior of the GDS, which grew in north-south width as it moved toward the equator, while its longitudinal size did not change (ignoring shape oscillations; Sromovsky et al., 1993).

Table 5. NDS-2018 size and aspect ratio.

Epoch	East-west width (km)		North-south width (km)		Aspect ratio		Major axis tilt
2018.69	10597	± 1834	4393	± 941	2.41	± 0.66	−14°
2018.85	10546	± 395	4109	± 206	2.57	± 0.16	−
2019.74	6285	± 212	3937	± 56	1.60	± 0.06	−
2020.02	6594	± 114	3709	± 39	1.78	± 0.04	6°
2020.48	6656	± 54	4019	± 28	1.66	± 0.02	4°
2020.63	6841	± 139	4048	± 129	1.69	± 0.06	−
2020.95	7031	± 69	3767	± 55	1.87	± 0.03	2°

NDS-2018 is the darkest spot ever seen on Neptune (Fig. 3d). The average contrast in 2020 of $-17 \pm 2\%$ is greater than the contrast of the GDS measured in Voyager's clear filter (–11%) or blue filter (–12%; Smith et al., 1989). Contrast is negative because the feature is dark rather than bright (Sec. B.4). The contrast of NDS-2018 measured in 2020 was much greater than the contrast at formation in 2018, and the contrast at every epoch after the September 2018 discovery data is greater than the contrast measured for the previous southern dark spot SDS-2015 (Wong et al., 2018) in the same WFC3 filters (Fig. 3d, inset).

The observations suggest that the major axis of NDS-2018 was inclined from an east-west orientation at some epochs, but the ability to measure this tilt with HST image quality is marginal. Table 5 lists the tilt (counterclockwise) of the major axis when we attempted to measure it during the 2D-Gaussian fitting procedure. For the 2018.69 epoch, the tilt of the dark area was measured by eye and is almost certainly affected by the presence of companion clouds. For epochs in 2020 when more than 8 frames per epoch were available (see Table 1), Table 5 reports the tilt measured on the coadded maps. We estimate uncertainties of ~0.6° for these values, based on the scatter of tilt measurements on the individual maps prior to coadding.

Observations of dark spot east-west drift rates (Fig. 4) find consistent offsets from the zonal wind field defined by tracking CH_4 ice clouds (e.g., Sromovsky et al., 1993). Dark spots may be vortices at deeper levels than the CH_4 ice clouds, but the vortices are not

expected to be passive tracers of the deeper flow. Instead, numerical models of anticyclones suggest that differences between vortex longitudinal drift rates and the background flow speed are influenced by atmospheric properties such as static stability, humidity, and vertical wind shear, as well as intrinsic properties such as vortex strength, vertical placement, and vertical extent (LeBeau and Dowling, 1998; Hadland et al., 2020). Drift rates are therefore an important element of the set of constraints available to narrow down the parameter space that numerical models need to span.
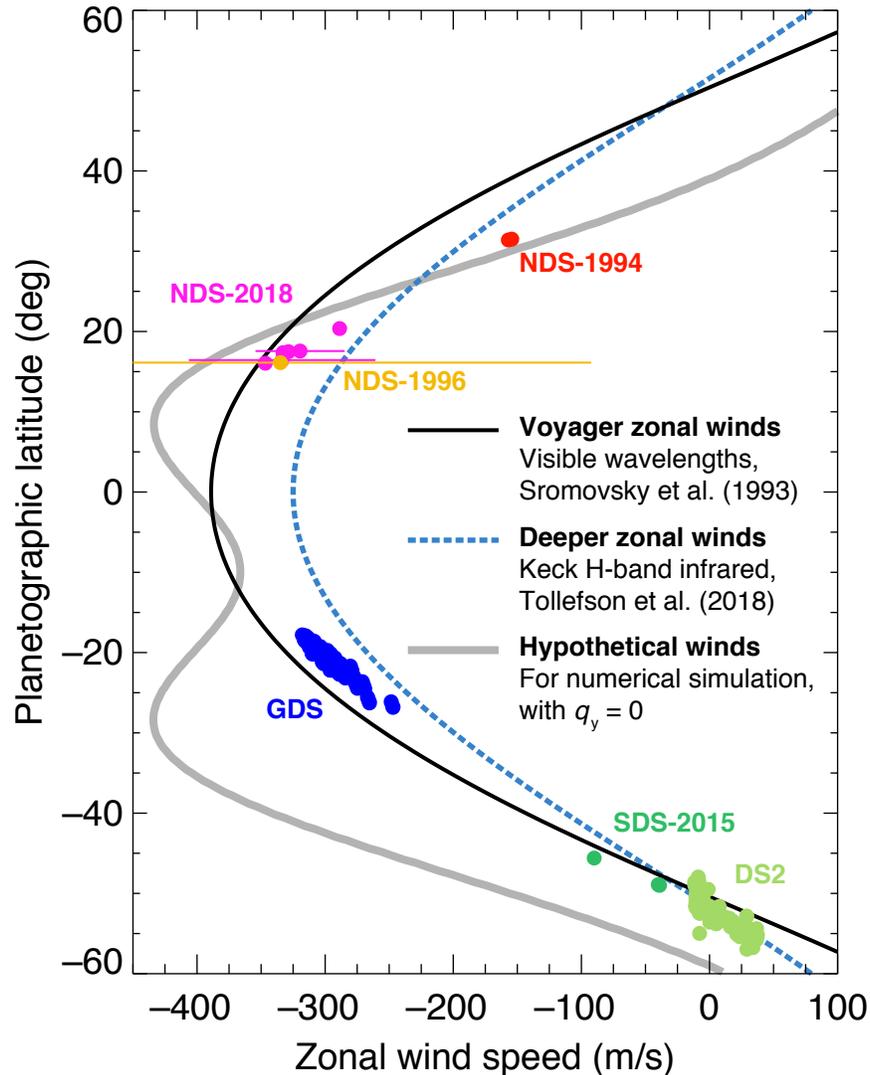
Fig. 4. Dark spot longitudinal drift compared to mean zonal winds. Observed drift rates of dark spots on Neptune (filled circles) depart from zonal wind profiles measured by tracking bright cloud features in visible-wavelength data (black curve; Sromovsky et al. 1993) and in H-band infrared data that may be sensitive to levels as deep as 3 bar (dashed curve; Tollefson et al., 2018). Vortex drift rates come from published data for GDS and DS2 (Sromovsky et al., 1993), NDS-1994 (Hammel and Lockwood, 1997), NDS-1996 (Sromovsky et al., 2001), and SDS-2015 (Wong et al., 2018). During the period that transient dark features were observed, NDS-2018 maintained a constant drift rate to within 2.5 m s^{-1} (Table 4, Sec. 3.3.3). An additional hypothetical wind profile designed to minimize q_y (the potential vorticity gradient) near the latitude of the NDS-2018 is shown in grey and discussed later in Section 3.3.

3. Results and discussion

3.1. Evolution of Neptune's six dark spots

We use the term "demise" to encompass different evolutionary pathways toward the end of the observable life cycle of vortices. We describe two alternate pathways for vortex demise: *dissipation* and *disruption*. Figure 5 gives evolutionary timelines of the six known dark vortices on Neptune. Due to the sparse temporal sampling of the observations, it is difficult to conclusively determine whether these dark spots dissipated or disrupted. There could be additional evolutionary pathways of vortex demise. Although disruption is a pathway favored in some simulations, observations are consistent with dissipation for three of Neptune's dark spots.
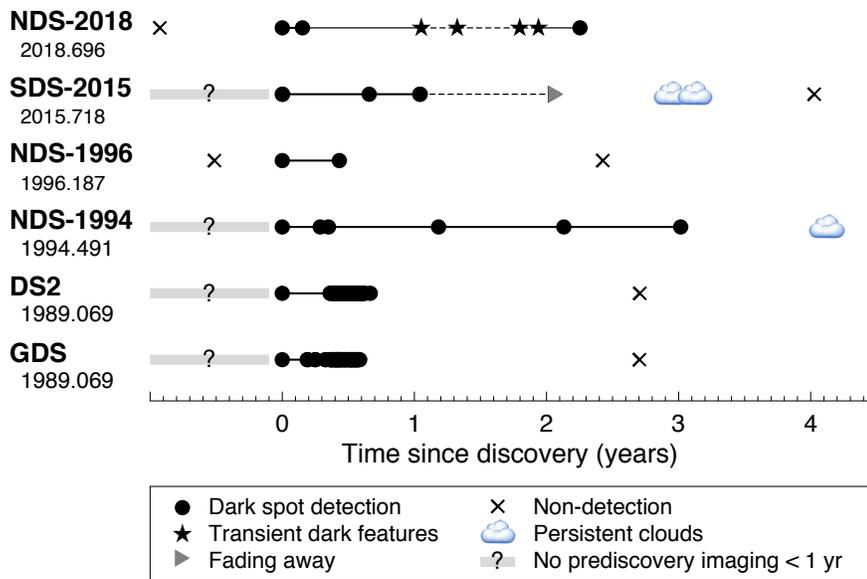
Fig. 5. **Observational coverage of Neptune's dark spots.** Prior Neptune dark spot observations did not cover the full lifespan of the observable vortices. Origin timing is marked by an "x" symbol representing a non-detection when available, or a "?" symbol when there is no available non-detection observation within one year of the discovery observation. Only two have well-defined origin timings. The "persistent clouds" symbol corresponds to observations where the dark spot itself was no longer seen, but compact clouds (perhaps companion clouds) were still seen near the last observed latitude of the dark feature. For vortex demise, both NDS-1994 and SDS-2015 observations are consistent with the dissipation pathway. The demise of the other three vortices (GDS, DS2, and NDS-1996) is not well-constrained because there was an interval of more than 1 year between the final observations of the features and a non-detection in imaging data. The presence of secondary dark features equatorward of NDS-2018 in 2019–2020 is indicated by stars. Fractional years near the vortex names give the time of their first observations. Published observation timeline data for GDS and DS2 are from Sromovsky et al. (1993), for NDS-1994 are from Hammel et al. (1995) and Sromovsky et al. (2001), for NDS-1996 are from (Sromovsky et al., 2001), and for SDS-2015 are from Wong et al. (2018), Simon et al. (2019), and Hsu et al. (2019).

Discussion of dark spot evolution involves a fair amount of speculation, due to the major gaps in the timelines of relevant observational data. It is possible that more pathways exist, or that both dissipation and disruption paths may combine. Uranus may demonstrate some of these ambiguities. Dark spots on Uranus are smaller than those on Neptune, may have shorter visible lifetimes, and are detectable at longer wavelengths (Hammel et al., 2009; Sromovsky et al., 2012). One feature, the Berg, was never seen directly as a dark spot on Uranus, but experienced latitude oscillations for years before drifting equatorward and disappearing (de Pater et al., 2011). The Berg was detected as bright cloud features suspected of being companions to an unseen dark vortex (de Pater et al., 2011; LeBeau et al., 2020), and the equatorward drift at the end of the feature's lifetime resembled the disruption pathway for Neptune vortices, although the invisibility of a dark spot itself resembled the dissipation pathway.

3.1.1.   Dissipation

The dissipation pathway is potentially relevant to three of Neptune's dark spots: DS2, NDS-1994, and SDS-2015. This type of vortex demise is not drawn from any specific theoretical prediction, but our review of observational trends discussed below suggest it is a likely outcome. The dissipation process may include observations of (1) a fading of dark spot contrast, (2) no significant equatorward drift, and (3) the persistence of centered companion clouds, even after the vortex itself is no longer visible. Due to the limited resolution of Earth-based observations, it is possible that both the fading and the persistent central clouds are related.

The persistence of possible companion clouds was observed for both NDS-1994 and SDS-2015. In observations less than one year after the last clear detections of these two dark spots, a small cloud feature was seen at the latitude where each vortex was last observed (Sromovsky et al., 2002; Hsu et al. 2019). For SDS-2015, companion clouds grew more centered over time, prior to the vortex becoming completely undetectable (Wong et al., 2018; Simon et al., 2019). Although the latitudinal position of the observed clouds is consistent with a vortex-companion cloud nature, it is not possible to determine whether the longitudinal positions are consistent with this interpretation due to the gaps in observational coverage. Demonstrating that observed cloud locations were within say 30° of the expected longitude of the dark spots would require drift rate precisions of 0.3 m s^{-1} over the relevant intervals of 404 days (NDS-1994) and 338 days (SDS-2015). The required precision is more than an order of magnitude smaller than our typical measured drift rate precisions (Table 4), and two orders of magnitude smaller than the typical time-variation in drift rates (Sromovsky et al. 1993, Wong et al. 2018). In the absence of high-cadence data, we rely on the coincident latitudes of the persistent cloud features as an admittedly weak basis for connecting them to the dissipating vortices.

A gradual fading of the dark spot—a reduction in contrast—was clearly measured for SDS-2015. In the WFC3 F467M bandpass, the contrast faded from $-6.6 \pm 0.8\%$ to $-2.9 \pm 0.4\%$ over a period of 2 years, from September 2015 to October 2017 (Wong et al., 2018). Estimation of the time rate of change in the contrast is difficult with limited temporal coverage; during a shorter period of just over 5 months in 2016, the absolute

contrast increased by 0.6%. However, this small intensification was not statistically significant.

Bright core clouds in DS2, observed throughout the Voyager 2 flyby (Smith et al., 1989), might represent a high-resolution look at the same dissipation pathway of vortex demise. DS2 remained within a 10° latitude band centered near 53°S for the entire period of Voyager coverage, with no hint of migrating towards the equator, where it could have been disrupted by vanishing Coriolis forces. Bright clouds in the core area were highly variable over duration of the Voyager coverage. The area and integrated relative brightness of the bright core clouds varied systematically with the latitudinal oscillation of DS2, with the core clouds reaching a brightness peak at the northernmost excursion (Fig. 10 of Sromovsky et al., 1993). If DS2 and its bright core clouds had been observed at HST spatial resolution (Fig. 6), detecting the dark spot itself may have been difficult or even impossible, depending on the contrast between the core clouds and the dark area. Although the limited temporal coverage during the Voyager 2 encounter could not determine whether DS2 faded and dissipated over its full lifetime, the possibility is strong that DS2, NDS-1994, and SDS-2015 shared similar evolutionary paths marked by a lack of equatorward drift and the presence of centered bright core clouds during their later stages.
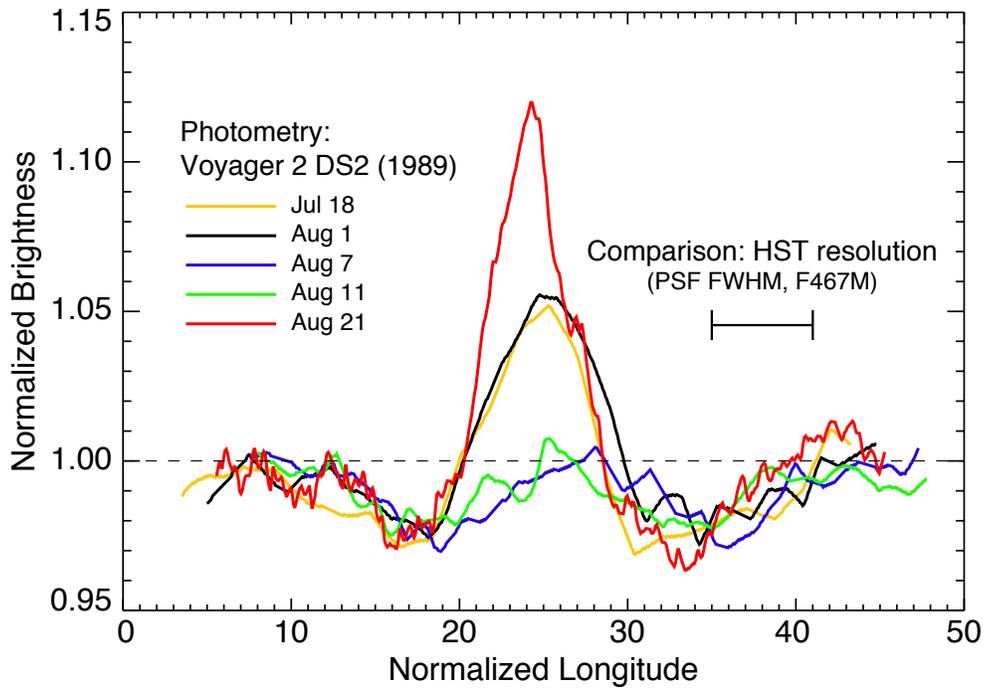

Fig. 6. Photometric scans across DS2 from Voyager imaging data. Voyager photometric scans show that DS2 was stable in contrast over a period of 20 days, but the central companion cloud's brightness varied significantly. If HST had been able to image this feature with current capabilities, the companion clouds would be clearly seen when bright, but the dark areas of DS2 would not have been well-resolved (scale bar gives resolution at typical geocentric distance at 55°S). All scans in the east-west directions were averaged over 1° latitude, across the vortex center (at planetographic latitudes −52.21°, −54.70°, −55.69°, and −53.20°, in chronological order). Images were acquired with the narrow-angle camera, using the clear filter, during approach to the planet. After closest approach (25 August, 1989), scans were not computed due to the high phase angles of the observations.

3.1.2.   Disruption

In contrast to the dissipation demise pathway (which is observationally suggested but not theoretically grounded), the disruption pathway is predicted by models but has never been directly observed. The disruption process is rooted in the expectation that anticyclonic vortices should drift equatorward due to the beta gyre effect (LeBeau and Dowling, 1998; LeBeau et al., 2020), if the background shear is anticyclonic (as shown by the empirical wind profiles in Fig. 4). Vortices in geostrophic balance remain coherent as the pressure gradient force is balanced by the Coriolis force, but near the equator, the Coriolis force vanishes and vortices are expected to become unstable. What vortex disruption may look like is not well defined, as the exact link between vortex structure and dark appearance is not fully understood. Simulated vortex disruption caused vorticity anomalies to expand over the full longitudinal domain (LeBeau and Dowling, 1998). Global-scale visible anomalies, either in terms of dark features or bright CH_4 ice cloud patterns, might be expected, but no such anomalies have been detected within the limits of existing temporal coverage.

We lack detailed observations of the formation of the secondary dark feature(s) observed in Fig. 2, and the cadence of observations is insufficient to determine whether the feature seen in the four epochs between Sept. 2019 and Aug. 2020 is a single feature, or separate features continuously generated over the 2019–2020 time period. The transient dark features were first seen as NDS-2018 approached the LeBeau and Dowling critical latitude for disruption. The surprising swerve of NDS-2018 away from the equator followed the detection of the secondary feature(s). By December 2020, NDS-2018 had again drifted equatorward, reaching its southernmost position to date (16.05° ± 0.07° S). No fainter dark features could be seen, despite the extremely high signal-to-noise level from multiple frames in this final epoch.

3.1.3.   Major-axis tilt
Measurements of a tilt between the major axis of NDS-2018 and the east-west direction (Table 5) are suggestive of shape oscillations seen in models (e.g., Polvani et al. 1990, LeBeau and Dowling 1998). Both the models and the Voyager imaging data (Polvani et al. 1990) showed that both the aspect ratio and the axial tilt of the GDS oscillated with the same period. We observe axial tilts of NDS-2018 in 2020 similar to the amplitude of the axial tilt oscillations of the GDS, ~10°. A larger tilt of –14° in the first observations of NDS-2018 is likely influenced by significant companion clouds in the HST imaging data. An accurate assessment of oscillations would require multiple samples over the period of the signal, which was about 200 hours for the GDS seen by Voyager (Polvani et al. 1990, Sromovsky et al. 1993). We have reliable tilt measurements only for three epochs in 2020, each following about 4000 hours after the last, which is insufficient to determine if oscillations are present (or to characterize their period, phase, and amplitude). The data do serve to demonstrate that WFC3 observations with ~8 or more image frames per HST orbit can provide sufficient accuracy to measure aspect ratio and axial tilt—if amplitudes are similar to the GDS oscillations observed by Voyager—but a higher observational cadence is required to determine if the shape of NDS-2018 is truly oscillating.

3.2. Global-scale dark regions

Dark regions extending across all longitudes of Neptune have been associated with some dark spots, but not the GDS. Voyager data show that DS2 was enveloped in a dark band (Smith et al., 1989), and the northern dark spots observed by HST/WFPC2, NDS-1994 and NDS-1996, were associated with a dark region that extended to the north (Sromovsky et al., 2001, 2002). This northern dark region brightened after the disappearance of the dark vortices (Karkoschka 2011). With the nature of dark spots and dark regions unknown (in terms of aerosol structure, composition, etc.), the nature of the association between these phenomena is also unknown. In particular, it is not clear whether dark spots somehow create dark bands, or whether dark bands mark atmospheric changes that promote the formation of dark spots.

Photometric profiles derived from HST/WFC3 data show that both SDS-2015 and NDS-2018 were associated with global-scale dark regions (Fig. 7). The disappearance of the southern dark band once SDS-2015 dissipated, and the onset of the dark region around the time of the formation of NDS-2018, both happened significantly faster than the 5–6 year time constants measured by Karkoschka (2011) for photometric changes in this wavelength range that were not clearly associated with dark spots. A difference between our analysis and that of Karkoschka (2011) is that we excluded image frames with dark spots present, while Karkoschka (2011) conducted a more comprehensive analysis and excluded regions with discrete bright features. Because bright features are very weak at blue wavelengths, the difference in approaches is expected to have minimal effects on the estimation of timescales of variability at the blue wavelengths studied here.

Scaling factors were used to match photometric profiles at each epoch to the mean reflectivity at 10°S–25°S in the 2020.9 data. This latitude range was chosen to calculate the scaling factors because the shape of the profile was identical at every epoch, and because Karkoschka (2011) found the least photometric variation in this region.

Global-scale dark regions are also observed in the absence of dark vortices, and the full range of factors influencing the zonal mean reflectivity of Neptune at blue wavelengths is not known. In particular, a dark band encircling the south polar region can be seen in Fig. 7b between about 67°–51° S; an extended bright feature with zonal wavenumber 1 at the northern edge of this dark band is visible as a bright/dark stripe from about 56°–51° S in the difference maps (Fig. 2). This dark band seems to be a more or less constant feature of the planet at blue wavelengths from the time of Voyager to the present day (Smith et al. 1989, Sromovsky et al. 2001, Karkoschka 2011), although the northern border extended equatorward to envelop DS2 when that spot was present. Latitudes between about 15° N and 30° N are often darker than other latitudes, but with low contrast and significant time variability (Smith et al. 1989, Karkoschka 2011). This region overlaps somewhat with the major global dark region that intensified in the 2018–2019 time range (Fig. 7), and with dark spots discovered in 1994 and 1996 (Hammel et al. 1995, Sromovsky et al. 2001). Dark bands and spots have been explained in one model as regions with a lower single-scattering albedo of particles in a deep H_2S ice layer ($P \geq 7$ bar; Irwin et al., 2022).
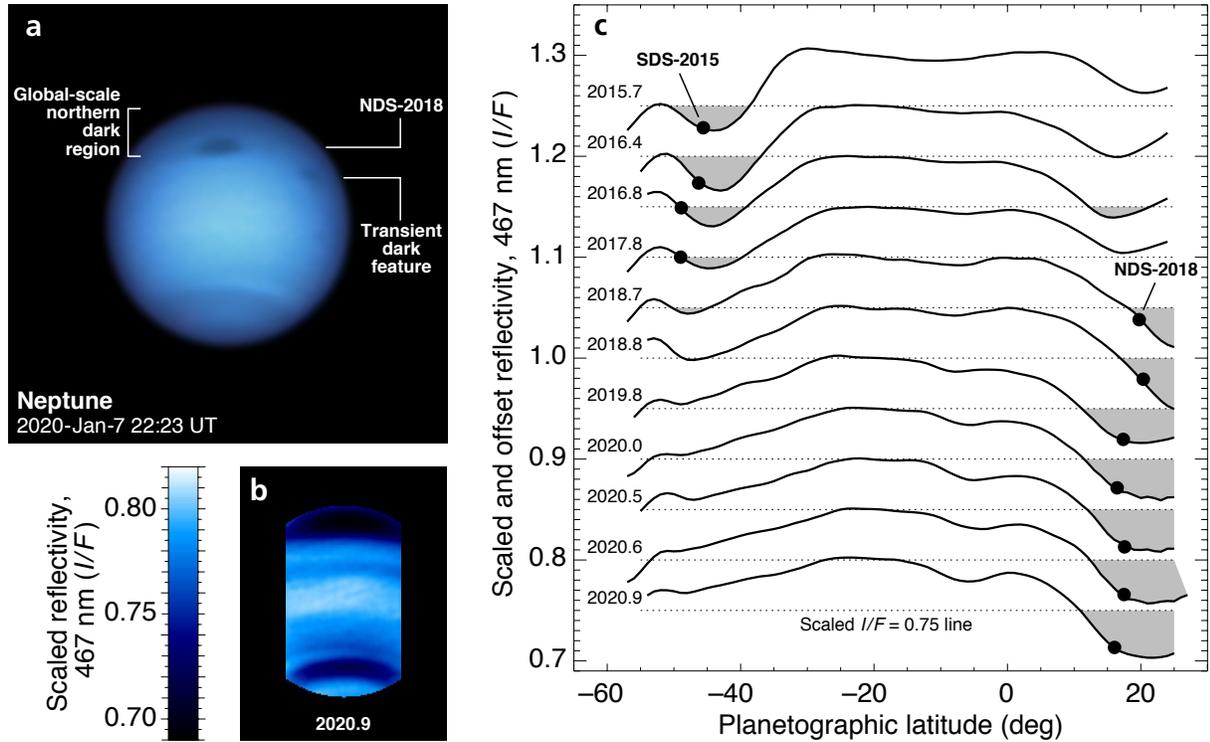
Fig. 7. Global-scale dark regions coincide with dark vortices. (a) A reconstructed color image of Neptune shows the discrete dark features in relation to the global-scale northern dark region in Jan. 2020. Limb darkening is preserved in this image, which includes data in filters at 467 nm, 547 nm, and 763 nm. Multiple frames were subsampled and stacked (after de-rotation to a common time point) to maximize image quality. **(b)** To compare photometric changes in the background atmosphere, data are corrected to first order for limb darkening using a Minnaert function with $k = 0.86$, selected to avoid frames with dark vortices present, restricted to emission angles $< 60°$, and restricted to projected central meridian distances $< 1/2$ the equatorial radius. An example of the data satisfying these selection constraints is shown for the 2020.9 epoch. In order to focus on localized changes in the photometric profiles, the I/F over the 10°S–25°S range for each epoch was scaled to match the 2020.9 value. **(c)** Meridional photometric profiles are shown for each epoch offset by 0.05 between each epoch (with the $I/F = 0.75$ level for each profile shown as a dotted line). Gobal-scale dark regions are associated with dark vortices: a dark band centered near 45°S– 50°S when SDS-2015 was present, and a widespread dark area to the north of NDS-2018. Shading indicates the locations of dark regions, which are close to the latitudes of contemporaneous dark spots (black points).

3.3. Simulations

We performed several numerical simulations with the Explicit Planetary Isentropic Coordinate (EPIC) model (Dowling et al., 1998; Dowling et al., 2006), to help interpret observations of the meridional drift of NDS-2018 and of transient dark features. To save time, we ran parallel simulations exploring different parameters using EPIC version 3.81 (triangle symbols in Fig. 8) and version 3.85 (circle symbols), with data files updated for Neptune initialization. The models were initialized with a vortex in a background anticyclonic shear at a latitude similar to NDS-2018 at the time of discovery, with varying vertical thicknesses and intrinsic strengths. Consistent with prior published works, we found that the strongest effects on drift rates came from variation in the atmospheric stratification, background meridional wind shear, and vortex strength.
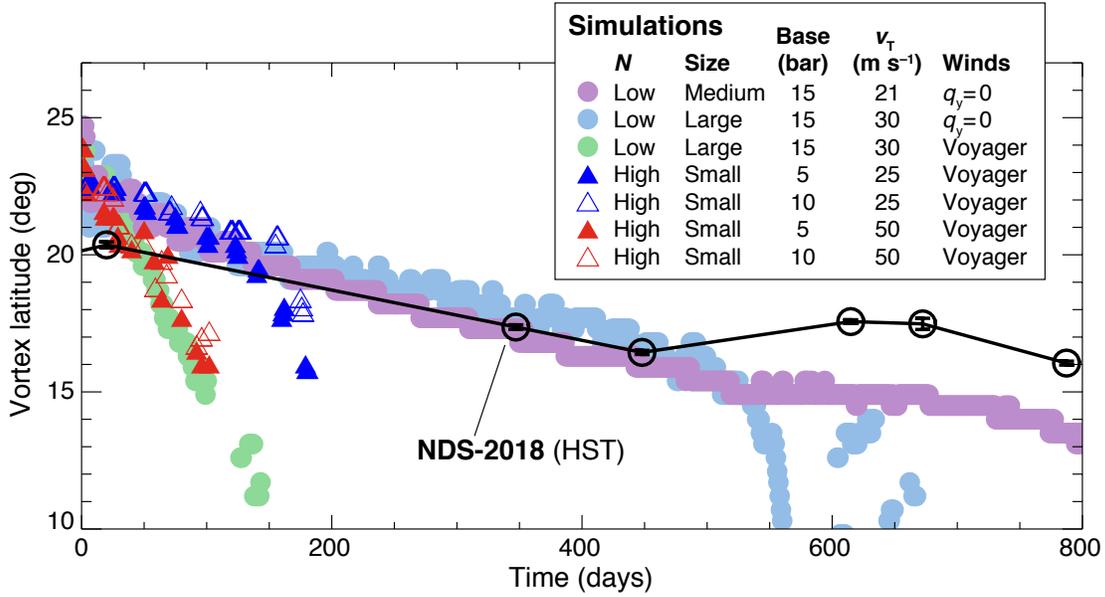
Fig. 8. Vortex meridional drift. Simulated vortices had faster equatorward drift rates than those observed for NDS-2018, except for cases with low static stability N, low $v_T \leq 30$ m s^{-1}, and a modified zonal wind profile featuring a near-zero absolute vorticity gradient (blue and purple circles). All other model cases used the Voyager wind profile (Sromovsky et al. 1993). All simulated vortices in high static stability environments (triangles) drifted faster. Model vortices disrupted or dissipated once they reached latitudes within 15° of the equator.

Our simulations neglect methane condensation and microphysics, potentially missing processes that may affect the latitudinal drift rates and oscillations of anticyclones as well as companion cloud formation (Deng et al. 2009, Hadland et al. 2020). For several of our simulations, we did include methane as a passive tracer, with an abundance that decreases with altitude near 1–2 bars but without condensation. Our treatment is similar to Stratman et al. (2001), who did not find differences in vortex dynamics when the deep methane abundance was varied. In dry models (without condensation processes), the main effect of including methane vertical variation is to increase the static stability, particularly near the methane ice condensation level. We explicitly vary the Brunt-Väisälä frequency N in our simulations, so some of the influence of methane humidity is wrapped up in this parameter.

The dynamic field is represented by the potential vorticity q which acts as a material tracer of the flow,

$$q = \frac{f+\zeta}{\rho} \frac{\partial \theta}{\partial z}$$

(1)

where ρ is the density, θ is the potential temperature, z the vertical coordinate, ζ is the relative vorticity, and $f = 2\,\Omega\,\sin(\phi)$ is the Coriolis parameter (Ω is Neptune's angular rotation rate, ϕ the latitude).

We initialize the anticyclone as an ellipsoid perturbation to the Montgomery potential (Stratman et al., 2001), with model domain, vortex, and model atmosphere parameter values listed in Table 6 and shown in Fig. 9. Parameters that were tested by different model cases were the tangential velocity (21, 25, 30, 50 m s^{-1}), vortex base pressure (5,

10, 15 bar), vortex size (bracketing the observed sizes in Fig. 3), Brunt-Väisälä frequency N (high and low, but both higher than the Voyager profile of Lindal, 1992), and wind profile (Figures 4 and 9). The high-N cases used a horizontal domain 8 times smaller than the low-N cases (120° × 30°, compared to 240° × 120°), but higher grid resolution (0.23° instead of 0.47°). The horizontal domains should be large enough so that periodic edge effects do not influence the simulated vortex behavior (see timestep 0 in Fig. 10). To test the effect of domain size on the results, we expanded the domain size for some of the low-N simulations (hollow triangle symbols in Fig. 8) by a factor of two in both horizontal directions, keeping all other parameters the same. The simulated vortex in these expanded-domain simulations had a faster drift rate, reaching 15°N and disrupting after 43 days. However, the same trend was preserved that faster tangential velocity leads to faster meridional drift. Since the objective of the exploratory modeling presented in this work is to identify trends in parameters rather than to isolate best-fit values, our conclusions are not strongly affected by the size of the model domain. In some of our earliest simulations of NDS-2018, we found slower drifts using a finer grid spacing of 0.11°, but we do not report results from these simulations in Fig. 8 because they used an even smaller domain and possibly insufficient vertical layers. Future long-duration simulations exploiting more computational resources may be needed to cover the entire globe at higher spatial resolution, to verify the requirements for domain independence minimum grid spacing.
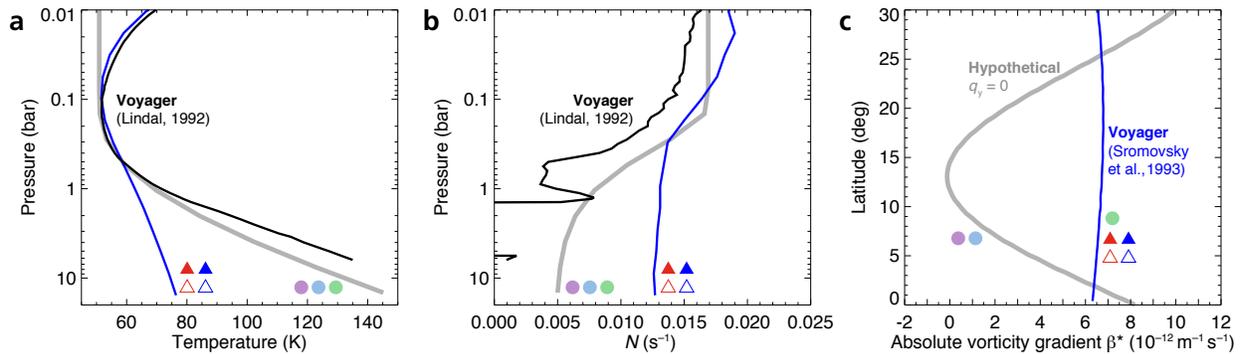

Fig. 9. Model atmospheres for the simulations. Symbols indicate profiles used for the simulations plotted in Fig. 8. **(a)** Temperature profiles for the low static stability cases (grey curve, circles) are similar to the Voyager temperature profile (Lindal, 1992) in the troposphere; simulations for the high static stability cases (blue curve, triangles) featured a shallower lapse rate. **(b)** Corresponding model Brunt-Väisälä frequencies N are compared with Voyager static stability (calculated using the CH_4 mixing ratio profile of Fletcher et al., 2014). **(c)** Background atmosphere vorticity gradients for all simulations corresponded to the Voyager zonal wind field (blue curve), except for the model cases indicated by blue and purple circles in Fig. 8. These cases use a hypothetical wind profile with near-zero potential vorticity gradient in the region of the vortex (grey curve), corresponding to the grey wind profile in Fig. 4.

Table 6. Model parameter space for Fig. 8.

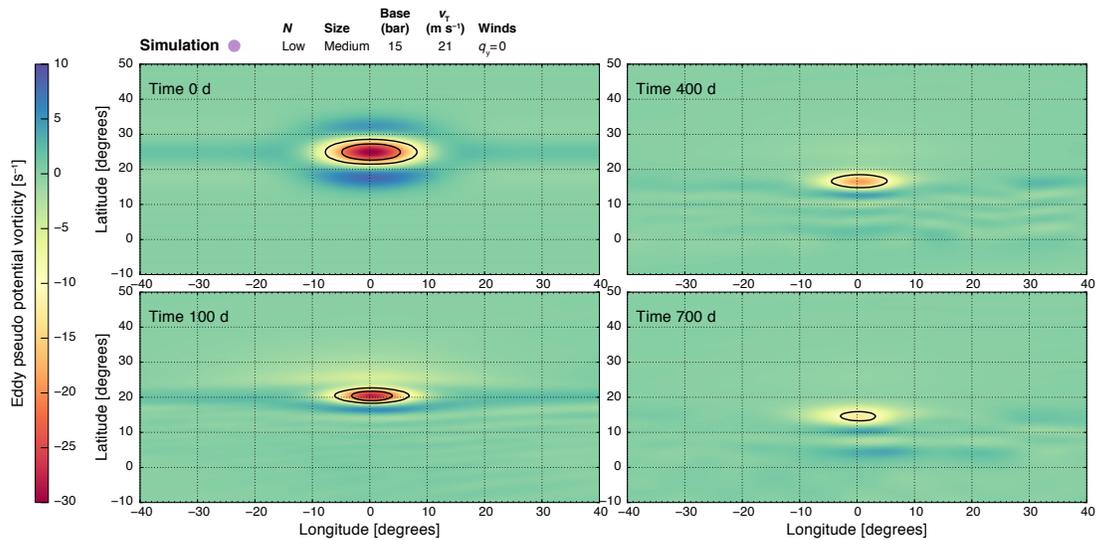|	Simulation	
Parameter	High-*N* (▲△▲△)	Low-*N* (●●●)
Vortex properties		
Full width (2a, 2b)	(13°, 6°)	(29°, 14°), (19°, 10.5°)
v_T (m s⁻¹)	25, 50	30, 21
Initial latitude	24°N	25°N
Top pressure (bar)	0.27	0.74
Midplane pressure (bar)	2	2
Bottom pressure (bar)	5, 10	15
Model domain		
Top pressure (mbar)	10	0.1
Bottom pressure (bar)	20	20
Vertical layers	25	20
Zonal extent	120°	240°
Meridional extent	0° to 30°N	60°S to 60°N
Horizontal resolution	0.23°	0.47°

Fig. 10. Simulated vortex evolution. Four timesteps within the single low-*N* simulation tracked by purple circles in Fig. 8. At initialization (time 0), cyclonic anomalies bordering the vortex emphasize the need for a large domain to avoid edge effects. At time 100 days, there is a large, diffuse northern anticyclonic anomaly to the north of the vortex. At later timesteps (400 and 700 days), the vortex decreases in strength and size. The late-stage evolution in the simulation seems to differ from observations that the vortex size and contrast remained constant (Fig. 3), but vorticity is not measured in the imaging data, so the unknown link between vorticity and visual appearance makes it difficult to compare observational and simulated results. The quantity mapped is the eddy (i.e., zonal-mean subtracted) pseudo-potential vorticity, as described in LeBeau and Dowling (1998).

The 20–25 vertical layers used in our simulations (with even spacing in log-pressure) is comparable to recent studies of Hadland et al. (2020; 35 layers) and LeBeau et al. (2020; 20 layers). The number of model layers between the vortex base and the lower boundary of the domain for the vortex base pressures tested—5, 10, and 15 bar—was 6, 3, and 1 respectively.

Our preliminary models include several simplifying assumptions, adopted for numerical convenience and computational speed, so more detailed simulations in the future may produce different results. We present simulations designed to provide initial interpretations of the observations, rather than definitive results. For example, past simulations of Neptune's Great Dark Spot aimed for a uniform potential vorticity region in the interior of the vortex (e.g., LeBeau and Dowling 1998), consistent with the vorticity distributions observed in Jupiter's Great Red Spot and White Ovals (e.g., Shetty et al. 2007, Wong et al. 2021), and with the basic Kida model used by Polvani et al. (1990) to explain the observed shape oscillations. Our study used Gaussian vortices which have a different internal distribution, potentially affecting drift rates and other parameters.

3.3.1. Migration and vortex strength

Equatorward migration is the expected behavior for an anticyclonic vortex on a rotating planet, due to the same beta gyre effect that often leads to poleward drift of cyclones like terrestrial hurricanes (Rossby, 1948; Adem, 1956). We modeled vortex drift (Fig. 8) using the standard Voyager wind profile (black curve in Fig. 4) as well as a hypothetical profile (grey curve in Fig. 4) with a potential vorticity gradient q_y near zero in the latitudes south of the vortex. This hypothetical profile follows prior studies demonstrating the sensitivity of vortex drift to the curvature (second derivative) of the zonal winds (LeBeau and Dowling, 1998; LeBeau et al. 2020). We measured vortex latitudes simply as the center of the elliptical vorticity anomaly at each timestep (triangle symbols in Fig. 8) or as the minimum eddy potential velocity in the domain (circle symbols).

The vortex in the $q_y = 0$ environment had a slower meridional drift, resembling that of NDS-2018, and it survived for a longer time before vortex demise. We were only able to test the hypothetical wind profile for two model runs with low static stability and low tangential velocity. Runs with higher static stability and/or faster v_T resulted in vortices with faster drift and disruption. These effects are additive; in simulations with the same Voyager wind profile and with high static stability, vortices with faster v_T (red triangles) had faster drift and disruption than vortices with with slower v_T (blue triangles). The large, low-N vortex (blue circle symbols in Fig. 8) decreased in size by a factor of about 2.5 over 560 days until it disrupted, and the medium, low-N vortex similarly decreased in size and strength over time (purple circle symbols in Fig. 8; Fig. 10). The size decrease in the simulations was greater than that observed for NDS-2018 (a factor of ~1.6) over a similar duration.

The link between slow migration and weak tangential velocity ($v_T < 50$ m s^{-1}) is plausible because slow drift is also linked to weaker vorticity in beta drift theory. Vortex strength can be represented by the vortex relative vorticity ζ_V or by v_T, with a relationship

dependent on the size and shape of the vortex (Hueso and Sánchez-Lavega, 2019) shown graphically in Fig. 11a for two different size/shape states of NDS-2018 (black and blue lines). Vortices with $v_T < 50$ m s^{-1} are some two to four times weaker (with respect to the background shear) than in prior simulations of Neptune vortices (LeBeau and Dowling, 1998; Polvani et al., 1990), although some Uranus vortex simulations came close to this range with v_T in the 30–50 m s^{-1} range (Deng et al. 2009, LeBeau et al. 2020). Strong vortices have vorticity ζ_V midway between the Coriolis parameter f (solid red line in Fig. 11a) and the background zonal wind shear ζ_B (dashed red line), as is the case for major vortices on Jupiter and Saturn (Legarreta and Sánchez-Lavega, 2005; García-Melendo et al., 2007).
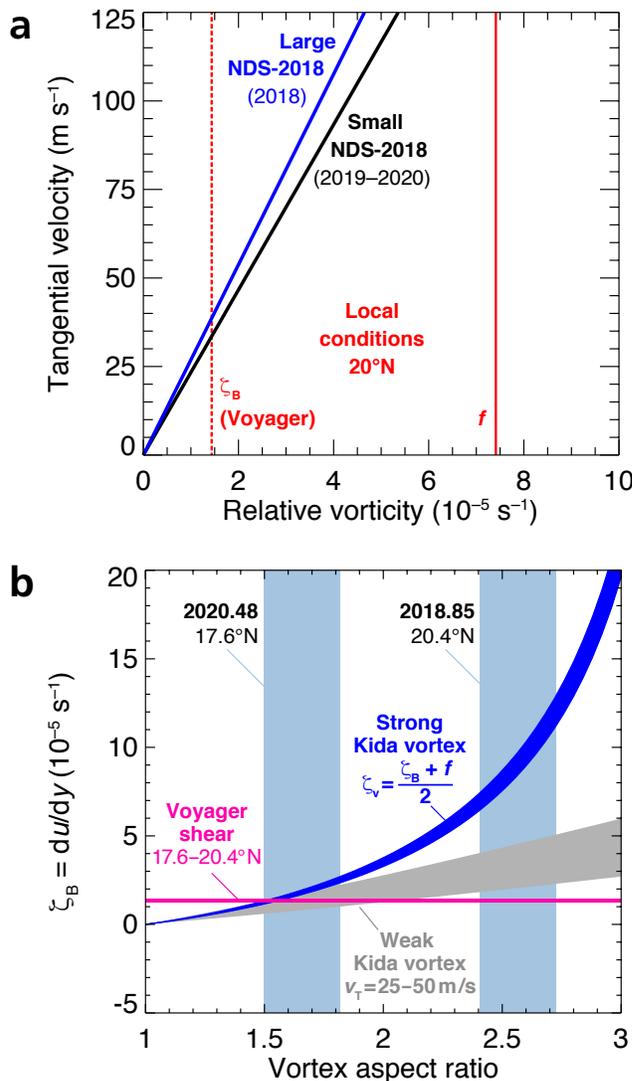

Fig. 11. Vortex strength. (a) Blue/black lines show the linear relationship between v_T and relative vorticity (Wong et al., 2018; Hueso and Sánchez-Lavega, 2019). The two lines span the size/shape variation of NDS-2018. Red lines show the planetary vorticity f (Coriolis parameter; solid) and the background vorticity (dashed) at 20°N. Strong vortices on Jupiter and Saturn would fall midway between these lines (Legarreta and Sánchez-Lavega, 2005; García-Melendo et al., 2007). If NDS-2018 were a strong vortex, it would have relative vorticity 4×10^{-5} to 5×10^{-5} s^{-1} and $v_T > 100$ m s^{-1}, resulting in a meridional drift faster than observations (see Fig. 8). **(b)** The observed vortex aspect ratio (shown in light blue for two epochs) are related to the wind shear in the environment (y-axis) by the Kida equations, producing the dark blue curve for the strong vortex case (Sromovsky et al., 1993; Wong et al., 2018; Hueso and Sánchez-Lavega, 2019; Simon et al., 2019), or the grey cuve for a weak vortex case wtih v_T fixed at 25–50 m s^{-1}. The 2018 aspect ratio is much more consistent with the Voyager environmental wind shear (Sromovsky et al. 1993) in the weak vortex case than in the strong vortex case.

3.3.2. Vertical shear

Studies of SDS-2015 (Wong et al., 2018) and NDS-2018 (Simon et al., 2019) suggested large vertical wind shear at the depth of the vortices, but these studies assumed a strong vortex. The inference of vertical wind shear comes from applying the Kida equations (Kida, 1981; Polvani et al., 1990; Hueso and Sánchez-Lavega, 2019), given the

background horizontal wind shear du/dy as a function of the observed vortex aspect ratios (light blue bands in Fig. 11b) and the vorticity. The strength of the vortex must be assumed, because direct measurements of the internal velocity field are not possible at HST angular resolution. For the strong vortex assumption (dark blue curve), the 2018 aspect ratio (near the time of the feature's origin) implies a horizontal shear some 5–10 times stronger than that of the Voyager zonal wind profile of Sromovsky et al. (1993). The wind shear discrepancy could be explained if the vortex was located at a deeper level than the cloud-tracked winds, in the presence of significant vertical wind shear. For the weak vortex assumption (grey band), the 2018 aspect ratio suggests a much lower horizontal wind shear, closer to the Voyager shear (within a factor of 3). Both the strong and weak vortex assumptions are consistent with the Voyager wind shear in the 2019–2020 time range, when the vortex shape was less eccentric (smaller aspect ratio). Application of the Kida model to NDS-2018 is a simplification of reality, because the Kida equations describe elliptical patches of uniform potential vorticity, and the exact relation between visible dark spot area and vorticity field is unknown in the absence of detailed wind field measurements in the vortex.

We also directly tested vertical wind shear using simulations where the background environments included vertical wind shear between 100 mbar and 4 bar. Vortices were sheared apart: horizontal slices through the simulation volume at different vertical layers contained coherent vortices at large horizontal displacements. The results resemble vertical fragmentation seen in prior fluid simulations (Achterberg and Ingersoll, 1994) even without vertical wind shear, although vertical fragmentation was only seen by Achterberg and Ingersoll (1994) when vortices were smaller than NDS-2018 by a factor of 3–5 (with size expressed in units of the deformation radius). Only a small number of vertical wind shear cases were tested in our limited simulations, with shear options designed to test strong vertical wind shear magnitudes suggested by prior analysis of the NDS-2018 aspect ratio (Simon et al. 2019). Conclusions drawn from these cases with vertical wind shear are qualitative, because these earlier simulations were conducted with limited vertical layers and horizontal domains (10 layers, 60°x15°) compared to our final simulations (Table 6). Future research is anticipated to contribute to this discussion (particularly testing weak vertical shear or different vertical distributions of shear with respect to the vortex vertical range), but our limited simulations provide some argument against the strong vertical shear implied by the Kida model for strong vortices (Fig. 11b and Simon et al. 2019).

3.3.3. Secondary features

Oscillations or reversals in latitude drift in the HST data (Fig. 3a) imply more complex interactions between NDS-2018 and its environment. It is intriguing to speculate that these interactions could relate to the transient dark features seen equatorward of the main dark spot. The transient dark features were first seen in September 2019, after which NDS-2018 reached its lowest latitude in January 2020, before it moved to higher latitudes in June and August of 2020. The sparse temporal sampling in the observations does not allow testing of the hypothesis that the latitudinal drift of NDS-2018 is related to the appearance of the transient dark features, as when a hot air balloon's altitude increases after dropping a ballast. Ongoing interactions between NDS-2018 and the specific

transient dark features detected in the HST data might not be expected at the large longitudinal offsets between the main vortex and the secondary features (> 45° in all observations, Fig. 2). Interactions at other epochs not observed could be possible, because the position of the transient dark features is consistent with a constant longitudinal drift rate of 86.3° per day, which differs from the 69.5°/day ± 0.5°/day drift of NDS-2018 over the 325-day period that the secondary dark features were observed (Table 4). The drift rate difference of 16.9°/day means that a single secondary dark feature at the observed longitudes would have lapped NDS-2018 around Neptune 15 times over 325 days. A single coherent feature persisting at such low latitudes for such a long time would be surprising, since LeBeau and Dowling (1998) found that vortices (initialized farther from the equator than NDS-2018) would drift equatorward and lose coherence at latitudes within about 15° of the equator (consistent with our simulations in Fig. 8). The nearly constant drift rate of NDS-2018 is remarkable given the observed spread in bright cloud features tracked by Voyager and ground-based observatories such as Keck (Limaye and Sromovsky 1991, Fitzpatrick et al. 2014, Tollefson et al. 2018).

Two issues arise when attempting to interpret the transient dark features through comparison with simulations. One is that simulations of an anticyclonic vortex may show a collection of transient secondary anticyclonic eddies, but the eddies are numerous, vary in shape over time, are scattered over the model domain, and are very short-lived (see Supplemental Movie S2). The distribution differs significantly from the observations, where only a single secondary dark feature was seen at each of four epochs distributed over a one-year period (with somewhat compact elliptical shape in the first two epochs and more irregular shape in the last two).

The second issue relating simulations and observations is that the link between anticyclonic vorticity (the simulation output) and low reflectivity in 400–550 nm images of Neptune (the observable quantity) is not well understood. Analysis of multispectral data suggests that dark spots and bands on Neptune correspond to darkening of particles deeper than levels of 3 bar (Karkoschka 2011) to 7 bar (Irwin et al. 2022). Currently there is no accepted theoretical basis for expecting anticyclonic vorticity to darken the particles in deep cloud layers. Vorticity tends toward zero over time in the simulations (Fig. 10), while the contrast of NDS-2018 (Fig. 3d) and the dark region to the north (Fig. 7c) increased over time. The simulations revealed large, diffuse northern anticyclonic anomaly covering a portion of the longitudinal domain (see 100 day timestep in Fig. 10), whereas the dark region observed on Neptune covers all longitudes. Future modeling studies may need to include aerosol processes in the H_2S-cloud layer in order to better link dynamical perturbations from models to aerosol perturbations from observations.

3.3.4. *Altitude change*

Did NDS-2018 change altitude as it evolved? The limited vertical resolution of our models cannot test this scenario, although the problem could be tackled by future simulations testing a wider range of vertical parameters (atmospheric structure, vertical shear, vortex vertical structure, humidity variation).

Still, the suggestion of altitude change arises from the low amount of companion cloud activity observed with NDS-2018, and the possibility that the vortex sampled different horizontal wind shears over time. Extensive companion clouds suggest that the vortex was at a deeper level in 2018 (Fig. 2; and Simon et al., 2019)—compared to 2019–2020 when no companion clouds were seen—because simulations found that deeper dark spots are associated with more extensive companion clouds (Stratman et al., 2001). More recent simulations including cloud microphysics and methane humidity paint a more complex picture of the parameters controlling companion clouds, including methane abundance and atmospheric thermal structure, with different types of companion clouds forming inside the bounds of the vortex and in the exterior (Hadland et al. 2020).

The strong Kida vortex case (dark blue curve in Fig. 11b) is consistent with a dark spot rising from a level with stronger zonal wind shear in 2018 to a level with wind shear similar to the standard Voyager profile in 2019–2020. But claims of vertical wind shear based on the strong Kida vortex assumption (Wong et al., 2018; Simon et al., 2019) must now be questioned, since the slow equatorward migration of NDS-2018 favors a weak vortex, at least in the small number of simulation runs reported here. Our evidence against significant vertical wind shear in the NDS-2018 environment is puzzling given the dispersion in wind speeds from cloud tracers tracked at different wavelengths (continuous and dashed lines in Fig. 4), which has been interpreted as a vertical wind shear effect (Tollefson et al., 2018). One possibility is that the vortex is confined to a deeper layer with no vertical wind shear, while the CH_4-ice clouds tracked by infrared imaging reside at higher levels with stronger vertical shear.

4. Conclusions

HST observations of NDS-2018 suggest that it is evolving along a disruption pathway (Sec. 3.1.2)—rather than a dissipation pathway as with some previous vortices (Sec. 3.1.1)—because the equatorward migration resembles previous simulations (LeBeau and Dowling, 1998; Hadland et al., 2020). Our new simulations suggest that equatorward drift could also be consistent with gradual dissipation (Fig. 10 and Supplemental Movie S2). NDS-2018 migrated equatorward after its initial formation, but its migration reversed (or oscillated) after the appearance of secondary dark features. Voyager observations of the GDS—another equatorward-migrating, high-contrast dark spot—also showed compact secondary dark features (Smith et al. 1989), although those were much smaller and would not have been detected by HST. Global-scale dark features associated with multiple dark spots (Fig. 7; Smith et al., 1989; Sromovsky et al., 2001, 2002) may have similarities to diffuse, large-scale anticyclonic anomalies to the north of the main vortex in some of our simulations. But there are major differences between the observations and our simulations; the large-scale eddy vorticity anomalies in our models did not extend over all longitudes, and their intensity faded over time.

Numerical simulations of the initial slow equatorward migration of NDS-2018 conclude that the tangential velocity is < 50 m s^{-1}, implying that the intrinsic vorticity of the dark spot is weak, only slightly more anticyclonic than the background flow. The longest-lived and slowest-drifting vortices in our simulations additionally were embedded in a low static stability environment, with a low meridional vorticity gradient inconsistent with the

standard Voyager zonal wind profile of Sromovsky et al. (1993). Conditions in Neptune's atmosphere are sufficiently unconstrained, and the parameter space exploration in our models is sufficiently coarse, that we cannot conclusively determine quantities like the stratification or wind profile. Rather, our initial exploratory work finds that the slow drift of NDS-2018 suggests that the static stability in the atmosphere is weaker rather than stronger, the tangential velocity is weak, and the zonal wind profile has a smaller curvature than the standard Voyager winds.

In simulations initialized with vertical wind shear, vortices were sheared apart. Earlier studies—assuming that Neptune's dark spots had strong vorticity—found horizontal wind shear different from the shear of the cloud-tracked mean zonal wind profile. The difference was interpreted as vertical wind shear (Wong et al., 2018; Simon et al., 2019; Hueso and Sánchez-Lavega, 2019), but when we use the weak vortex assumption in the Kida equations, we no longer require vertical wind shear to match the observations (i.e., wind shear at the level of the dark spot is consistent with wind shear of the cloud-tracked mean zonal wind profile). One of the challenges of modeling the background flow in the vortex environment is the uncertainty in the actual wind shear, with observations showing high levels of dispersion among individual wind measurements with respect to the average flow (e.g., Limaye and Sromovsky, 1991; Fitzpatrick et al., 2014; Tollefson et al., 2018). The relevance of a single zonal wind profile in modeling the background flow may be called into question, especially because the relative contributions from longitudinal variation (e.g., waves and eddies), temporal variation, and vertical shear are not well defined.

Several anticyclones on Jupiter and Saturn have measured relative vorticities considerably stronger than the background flow, as constrained by spacecraft and HST imaging with spatial resolution, dynamic range, and temporal sampling not available for observations of Neptune. It is unclear why NDS-2018 on Neptune may be weaker than anticyclones on Jupiter and Saturn, or whether NDS-2018 is representative of other Neptune dark spots, or an outlier. Many other puzzles remain, because it is unknown how dark spots are created, or what controls their size and vertical extension. New high-cadence observations—from a Neptune orbiter (Hueso and Sánchez-Lavega, 2019) or a vantage point at the Earth capable of achieving sufficient contrast and resolution (Wong et al., 2009; Young et al. 2021)—would spark a renaissance in the understanding of vortex dynamics. Despite the sparseness of the existing observations of NDS-2018 described here, the observational history of this feature is the most complete of any dark vortex on Neptune in the post-Voyager era. While this study covered the period from discovery in 2018 through the end of 2020, HST observations of Neptune in 2022 show the continuing presence of NDS-2018, with fading contrast. These results will be described in a later paper.

Acknowledgements

Data and code availability

Raw and calibrated HST imaging data are available from the MAST archive, https://archive.stsci.edu, by searching program IDs listed in Table 1. Voyager data can be retrieved using the PDS Ring-Moon Systems Node's OPUS search service (https://opus.pds-rings.seti.org). The EPIC fluid dynamics source code is available from the PDS Atmospheres node, https://atmos.nmsu.edu/data_and_services/software/epic/epic.htm, with a recent compiler compatibility update posted at GitHub, https://github.com/LJOPA/epic. Maps and individual image frames from Fig. 2 are available from MAST (Wong 2022).

Appendix A. Hubble observations and processing

Neptune's dark spots are notoriously difficult to observe because they require high resolution (spanning only about 0.3"), and they can only be detected at blue visible wavelengths (Smith et al. 1989; Hammel et al., 1995; Wong et al., 2018, Sánchez-Lavega et al., 2019), where ground-based adaptive optics or speckle imaging techniques have not yet achieved high enough image quality, particularly on complex extended sources. HST therefore is uniquely capable of observing dark spots.

A 512×512-pixel subarray was used for Neptune observations to maximize the number of frames per HST orbit, by minimizing detector readout time and buffer dump frequency. The extended scattered light halo around Neptune was sufficient to compensate for charge transfer inefficiency losses (see Fig. 2 in Wong et al., 2020), so we did not post-flash the exposures. Program numbers (which can be used to access raw data from the MAST archive) are listed in Table 1. Most of the epochs of observation correspond to the

annual OPAL program. Additional programs listed (at epochs 2020.02, 2020.49, and 2020.95) were specifically designed to image NDS-2018, so these programs included higher numbers of F467M exposures in every HST orbit. These focused NDS-2018 programs were also able to employ more extensive dithering, an important strategy to make up for pixel-to-pixel noise, especially including cold unstable pixels (Borque et al., 2018). Our dithering approaches combine traditional dithering from telescope pointing offsets, as well as rotational dithering achieved by multiple images at differing target rotational phase.

Some HST orbits were either partially or completely lost, when guide star lock was lost (or never achieved) and fast pointing drift caused the images to be blurred or the target to be out of the subarray field of view. It is unclear to what extent these loss-of-lock (LOL) events were caused by instability of the HST gyroscopes. Hubble is now operating in three-gyroscope mode with no remaining backup gyroscopes (see Wong et al., 2020 for a discussion of the HST gyroscope history in the era after Servicing Mission 4). Regardless of the cause, the LOL failures resulted in a fortuitous set of bonus observations in 2018. The original OPAL observations (epoch 2018.70) captured the first images of NDS-2018, but at a very high emission angle near the limb of the planet. Repeat observations were granted (epoch 2018.85), capturing the dark spot at a better viewing angle and revealing significant changes in companion cloud activity over only a short timespan of two months.

Images acquired in the F467M filter of WFC3 (Dressel, 2021) are used for tracking and measuring vortex morphology, because this filter gives the best feature contrast at reasonable exposure times (Wong et al., 2018). Neptune's extreme distance and strong limb darkening at blue wavelengths means that the dark spot is difficult to see in single images, and the finer aspects of feature morphology are not resolved. Rather than operate on data corrected for limb darkening using the Minnaert function (Wong et al., 2018; Hsu et al., 2019), we subtract background images of Neptune to create "difference images" (Sromovsky et al., 2001).

The global difference maps shown in Fig. 2 exhibit varying levels of graininess due to the different numbers of individual frames stacked at each epoch (Table 1). The observational epochs with the highest image quality in Fig. 2 correspond to very large numbers of individual image frames (up to 28).

Data processing steps included correction for cosmic ray defects using the LA-Cosmics approach for single frames (van Dokkum, 2001), and corrections for fringing in the long-wavelength narrowband filter FQ727N (Wong, 2011). The fringing corrections are relevant only to observations of companion cloud features, since the dark spot itself can only be seen at short wavelengths, where there is no fringing in the WFC3/UVIS bandpass. To correct for scattered light in the extended halo of the HST point spread function (PSF), we deconvolved the data with the TinyTim PSF and reconvolved them with an idealized PSF lacking extended wings (Sromovsky and Fry, 2002). The raw images were then corrected for geometric distortion using the detector solutions from Martlin et al. (2018), and mapped to planetary coordinates using the Simnav method (Wong et al., 2020). At this step, the imaging data are magnified (with bicubic interpolation) by a factor of 2–3, facilitating recovery of subpixel image resolution during

subsequent coaddition processes. This is necessary because the WFC3/UVIS pixel sampling (0.039"/pixel) does not fully sample the HST PSF at Nyquist frequency (0.068" FWHM in F467M, Dressel, 2021). Finally, the data were converted to non-dimensional *I/F* reflectivity units by dividing by range-corrected solar flux. These processed and navigated data products (with geometrical backplanes) are available at the MAST archive (Wong 2022).

For each epoch, the difference images rely on stacks of individual frames for the background "B-frames." Our global observations produce a factor of ~3–6 more B-frame data (compared to the A-frame data showing the dark spot itself), depending on factors such as the presence of other dark features besides NDS-2018 in a particular epoch, the position of NDS-2018 on the disk (centered in a single HST orbit vs. off-center in two HST orbits), and the availability of two rotations of Neptune data that can be stacked together (this excludes 2020.02 and 2020.49 epochs). The higher number of frames in the B-frame stacks ensures that the SNR of the difference images is not significantly higher than that of the A-frame images and stacks themselves, since the dominant source of error in our imaging data is transient pixel-to-pixel variation that is not well corrected by the WFC3 calibration pipeline flat-fielding operation. Another possible error source in the difference images, which appears to be small at the low latitudes of interest, is non-uniformity in background clouds, such as the bright and dark streaks near 55° S.

Our analysis used both individual difference images, and stacked difference images combining multiple frames. Since the longitudinal drift rate of NDS-2018 is fast (Fig. 4), we only included frames from within a single HST orbit in the stacked difference images. For several epochs, the drift rate of the vortex could be accurately measured, particularly when two rotations of Neptune were imaged. At these epochs, we additionally worked with shifted stacked difference images, created by shifting individual map frames to the moving reference frame of NDS-2018.

Appendix B. Morphological measurements

Figure 1e–1f gives an example of a difference map and its corresponding 2D Gaussian fit, and Figure 1g–1h shows photometric scans along the east-west and north-south axes through the center of the fitted Gaussian profile. We generally derive morphological and positional parameters from the fits to stacked difference maps, and empirically estimate errors using the scatter from similar fits to individual difference images. For epochs with good image quality (8 or more frames showing NDS-2018), the Gaussian fit included a variable inclination of the major axis with respect to the east-west direction, as reported in Table 5. For epochs with fewer frames, the Gaussian fit was performed assuming that the major axis was in the east-west direction. Details differ for each morphological parameter derived from these Gaussian fits, as described below.

B.1. Major width

The major width is defined as the full width at half maximum (FWHM) of the 2D Gaussian fit along the major axis of the ellipse, equivalent to the east-west width for an ellipse aligned with the planetary coordinates. In this direction, the NDS-2018

photometric profile has a flat bottom, creating a broader peak than the Gaussian function. Optimized Gaussian fits therefore tend to have lower peak values (higher absolute difference value) compared to the observations, and higher values (lower absolute difference values) on the slopes of the profile where the FWHM is measured. The fits therefore underestimate the true major width of the feature by a small amount. This underestimation is consistent from epoch to epoch since the same methodology was used, so relative changes in major width (and aspect ratio) are not significantly affected by this shape error.

The Gaussian fit includes a term for the baseline, so it is not assumed that the *I/F* difference is zero away from NDS-2018. In the example of Fig. 1, the residuals show that the *I/F* difference just south of NDS-2018 was darker than north of the feature, and the region just to the east of the vortex was also darker. These are very faint differences that are only revealed by the large number of F467M frames taken per orbit at the 2020.95 epoch.

For the September 2018 data, only two frames showed NDS-2018, very close to the limb. There was also significant companion cloud activity close to (and perhaps overlapping) the vortex at this epoch. Uncertainty was also introduced by an ambiguity between two possible shapes consistent with the imaging data: an elliptical shape aligned ~14° clockwise from the east-west direction, or an elliptical shape aligned east-west but partially obscured by companion clouds. The 2D Gaussian fitting procedure failed on these very challenging observations, so fits were done by hand. Error bars shown in Fig. 3abc include the ambiguity in shape interpretations.

B.2. Minor width

The minor width is similarly defined as the FWHM along the minor axis of the ellipse, equivalent to the north-south width for an aligned elliptical vortex. Although the vortex photometric profile is closer to a Gaussian shape in the minor axis direction, Fig. 1h still shows an example where the observed peak is broader than a Gaussian shape. Again, the size may be slightly underestimated due to the Gaussian shape assumption, but the non-Gaussian error will be smaller than that in the major axis direction.

B.3. Longitude and latitude

The longitude and latitude of the feature center is defined as the center of the fitted 2D Gaussian profile. The latitude of the center was assumed to be constant for all frames during each individual epoch, so central latitude can be measured on stacked difference maps, with the uncertainty given by the standard deviation of central latitudes measured on individual frames, divided by $N^{0.5}$, where N is the number of frames. But longitude varies with time, so central longitudes of individual frames were instead used to define a linear rate of longitudinal drift, and the standard deviation of the longitude residuals (divided by $N^{0.5}$) was used to estimate the uncertainty in the drift rate at each epoch. Error bars shown in Fig. 4 are much smaller when observations are available over two Neptune rotations, assuming a linear rate of drift over the individual frames in each epoch.

B.4. Central contrast

The central contrast C is defined (Wong et al., 2018) as the normalized difference in I/F between the vortex and its surroundings:

$$C = \frac{I/F_{\text{DS}} - I/F_{\text{surr.}}}{I/F_{\text{surr.}}} \tag{2}$$

The contrast of a dark feature is thus a negative number, but we use wording like "the contrast increased" to mean that C became a more negative number. Previous calculations of C modeled limb darkening using a Minnaert function (Wong et al., 2018), but in the current work, we instead calculate the numerator from difference images uncorrected by the Minnaert function (e.g., Figs. 1c and 1d), and the denominator from the smooth background disk image (Fig. 1b). Values of C calculated by these two methods can be directly compared, since the Minnaert correction is a multiplicative factor that cancels out in Equation 2.

To calculate the central contrast at each epoch, we first determined the dark spot position and size as described above and estimated the time-dependent longitude in each frame when drift rates could be estimated. We then isolated the central region of NDS-2018 in each frame for sampling. The sampling core was taken to have the same aspect ratio as the vortex itself, but only 1/3 the size in linear dimensions. The contrast at each epoch was then taken as the minimum value within the sampling core, averaged over the available frames. Core sampling was used rather than the amplitude of the 2D Gaussian fits because the fits tend to overestimate the depth of the photometric anomaly (Gaussian brightness profiles don't match the observed flat bottom). Because the central contrast is measured using a smaller total number of pixels than the morphological properties listed above, it is more strongly affected by pixel-to-pixel noise in the WFC3 detector. Accounting for this noise effect is difficult, so we estimated the uncertainty in the central contrast as the root sum of squares of two quantities: the standard deviation of the minimum contrast point in the sampling cores of all individual frames at each epoch, and the standard deviation of the mean contrast in the sampling cores of all the frames.

Appendix C. Supplementary data

MMC S1. Table S1. NDS-2018 and secondary dark feature sizes in angular units (latitude/longitude). This is the same information given in Fig. 3c. Values are converted from the information in Tables 2 and 5 in linear units (km).

MMC S2. Movie of the simulation that is marked in Fig. 8 by purple dots. Several frames from this simulation are shown in Fig. 10.

References

Achterberg, R.K., and A.P. Ingersoll. 1994. "Numerical Simulation of Baroclinic Jovian Vortices." *Journal of the Atmospheric Sciences* 51: 541-562.

Adem, J. 1956. "A Series Solution for the Barotropic Vorticity Equation and its Application in the Study of Atmospheric Vortices." *Tellus* 8: 364–372.

Borque, M., D. Borncamp, S. Baggett, T. Desjardins, and N. Grogin. 2018. *WFC3 Instrument Science Report 2018-15:* Using Dark Images to Characterize Pixel Stability in the WFC3/UVIS Detector. Baltimore, MD: Space Telescope Science Institute.

Deng, X., R. LeBeau, and C. Palotai. 2009. "Numerical Investigation of Orographic Cloud and Vortex Dynamics on Ice Giant Planets." *American Institute of Aeronautics and Astronautics Atmospheric and Space Environments Conference Proceedings* 2009: 3643 (23 pp.). DOI: 10.2514/6.2009-3643

de Pater, I., L. A. Sromovsky, H. B. Hammel, P. M. Fry, R. P. LeBeau, K. Rages, M. Showalter, and K. Matthews. 2011. "Post-equinox observations of Uranus: Berg's evolution, vertical structure, and track towards the equator." *Icarus* 215: 332–345.

Dowling, T. E., A. S. Fischer, P. J. Gierasch, J. Harrington, R. P. LeBeau, and C. M. Santori. 1998. "The Explicit Planetary Isentropic-Coordinate (EPIC) Atmospheric Model." *Icarus* 132: 221-238.

Dowling, T. E., M. E. Bradley, E. Colón, J. Kramer, R. P. LeBeau, G. C. H. Lee, T. I. Mattox, R. Morales-Juberías, C. J. Palotai, V. K. Parimi, and A. P. Showman. 2006. "The EPIC atmospheric model with an isentropic/terrain-following hybrid vertical coordinate." *Icarus* 182: 259-273.

Dressel, L. 2021. *Wide Field Camera 3 Instrument Handbook, Version 13.0*. Baltimore, MD: Space Telescope Science Institute.

Fitzpatrick, P.J., I. de Pater, Luszcz-Cook, S., M.H. Wong, and H.B. Hammel. 2014. "Dispersion in Neptune's zonal wind velocities from NIR Keck AO observations in July 2009." *Astrophysics and Space Science* 350: 65-88.

Fletcher, L.N., I. de Pater, G. S. Orton, H.B. Hammel, M.L. Sitko, and P.G.J. Irwin (2014) "Neptune at summer solstice: Zonal mean temperatures from ground-based observations, 2003-2007." *Icarus* 231: 146–167.

García-Melendo, E., A. Sánchez-Lavega, and R. Hueso. 2007. "Numerical models of Saturn's long-lived anticyclones." *Icarus* 191: 665-677.

Hadland, N., R. Sankar, R.P. LeBeau, and C. Palotai. 2020. "EPIC simulations of Neptune's dark spots using an active cloud microphysical model." *Monthly Notices of the Royal Astronomical Society* 496: 4760-4768.

Hammel, H.B., and G.W. Lockwood. 1997. "Atmospheric Structure of Neptune in 1994, 1995, and 1996: HST Imaging at Multiple Wavelengths." *Icarus* 129: 466-481.

Hammel, H. B., L. A. Sromovsky, P. M. Fry, K. Rages, M. Showalter, I. de Pater, M. A. van Dam , R. P. LeBeau, and X. Deng. 2009. "The Dark Spot in the atmosphere of Uranus in 2006: Discovery, description, and dynamical simulations." *Icarus* 201: 257–271.

Hammel, H. B., R. F. Beebe, E. M. de Jong, C. J. Hansen, C. D. Howell, A. P. Ingersoll, T. V. Johnson, S. S. Limaye, J. A. Magalhaes, J. B. Pollack, L. A. Sromovsky, V. E. Suomi, and C. E. Swift. 1989. "Neptune's wind speeds obtained by tracking clouds in Voyager images." *Science* 245: 1367-1369.

Hammel, H.B., G.W. Lockwood, J.R. Mills, and C.D. Barnet. 1995. "Hubble Space Telescope Imaging of Neptune's Cloud Structure in 1994." *Science* 268: 1740-1742.

Hsu, A.I., M.H. Wong, and A.A. Simon. 2019. "Lifetimes and Occurrence Rates of Dark Vortices on Neptune from 25 Years of Hubble Space Telescope Images." *The Astronomical Journal* 157: 152 (9 pp.).

Hueso, R., and A. Sánchez-Lavega. 2019. "Atmospheric Dynamics and Vertical Structure of Uranus and Neptune's Weather Layers." *Space Science Reviews* 215: 52 (33 pp.).

Irwin, P.G.J., N.A. Teanby, L.N. Fletcher, D. Toledo, G.S. Orton, M.H. Wong, M.T. Roman, S. Perez-Hoyos, A. James, and J. Dobinson. 2022. "Hazy blue worlds: A holistic aerosol model for Uranus and Neptune, including Dark Spots." *Journal of Geophysical Research: Planets*, in press. DOI: 10.1029/2022JE007189

Karkoschka, E. 2011. "Neptune's cloud and haze variations 1994-2008 from 500 HST-WFPC2 images." *Icarus* 215: 759-773.

Kida, S. 1981. "Motion of an elliptic vortex in a uniform shear flow." *Journal of the Physical Society of Japan* 50: 3517-3520.

LeBeau, R.P., and T.E. Dowling. 1998. "EPIC Simulations of Time-Dependent, Three-Dimensional Vortices with Application to Neptune's Great Dark Spot." *Icarus* 132: 239-265.

LeBeau, R.P., K. Farmer, R. Sankar, N. Hadland, and C. Palotai. 2020. "A Numerical Investigation of the Berg Feature on Uranus as a Vortex-Driven System." *Atmosphere* 11: 52 (11 pp.).

Legarreta, J., and A. Sánchez-Lavega. 2005. "Jupiter's cyclones and anticyclones vorticity from Voyager and Galileo images." *Icarus* 174: 178-191.

Limaye, S.S., and L.A. Sromovsky. 1991. "Winds of Neptune: Voyager observations of cloud motions." *JGR* 96: 18941-18960.

Lindal, G. F. 1992. "The Atmosphere of Neptune: an Analysis of Radio Occultation Data Acquired with Voyager 2." *The Astronomical Journal* 103: 967–982.

Marcus, Philip S. 1990. "Vortex dynamics in a shearing zonal flow." *Journal of Fluid Mechanics* 215: 393-430.

Martlin, C., V. Kozhurina-Platais, M. McKay, and E. Sabbi. 2018. *WFC3 Instrument Science Report 2018-10:* Updates to the WFC3/UVIS Filter-Dependent and Geometric Distortions. Baltimore, MD: Space Telescope Science Institute.

Polvani, L.M., J. Wisdom, E. DeJong, and A.P. Ingersoll. 1990. "Simple dynamical models of Neptune's Great Dark Spot." *Science* 249: 1393-1398.

Rossby, C.G. 1948. "On displacement and intensity changes of atmospheric vortices." *Journal of Marine Research* 7: 170-196.

Sánchez-Lavega, A., L.A. Sromovsky, A.P. Showman, A.D. Del Genio, R.M.B. Young, R. Hueso, E. García-Melendo, et al. 2019. "Gas Giants." In *Zonal Jets: Phenomenology, Genesis, and Physics*, 72-103. Cambridge: Cambridge University Press.

Simon, A.A., M.H. Wong, and A.I. Hsu. 2019. "Formation of a New Great Dark Spot on Neptune in 2018." *Geophysical Research Letters* 46: 3108-3113.

Simon, A.A., M.H. Wong, and G.S. Orton. 2015. "First Results from the Hubble OPAL Program: Jupiter in 2015." *The Astrophysical Journal* 812: 55 (8 pp.).

Smith, B. A., and 64 colleagues. 1989. "Voyager 2 at Neptune: Imaging Science Results." *Science* 246: 1422-1449.

Sromovsky, L. A., H. B. Hammel, I. de Pater, P. M. Fry, K. A. Rages, M. R. Showalter, W. J. Merline, P. Tamblyn, C. Neyman, J.-L. Margot, J. Fang, F. Colas, J.-L. Dauvergne, J. M. Gómez-Forrellad, R. Hueso, A. Sánchez-Lavega, and T. Stallard. 2012. "Episodic bright and dark spots on Uranus. "*Icarus* 220: 6–22.

Sromovsky1993, L.A., S.S. Limaye, and P.M. Fry. 1993. "Dynamics of Neptune's Major Cloud Features." *Icarus* 105: 110-141.

Sromovsky, L.A., S.S. Limaye, and P.M. Fry. 1995. "Clouds and circulation on Neptune: Implications of 1991 HST observations." *Icarus* 118: 25-38.

Sromovsky, L.A., P.M. Fry, T.E. Dowling, K.H. Baines, and S.S. Limaye. 2001. "Coordinated 1996 HST and IRTF Imaging of Neptune and Triton. III. Neptune's Atmospheric Circulation and Cloud Structure." *Icarus* 149: 459-488.

Sromovsky, L.A., and P.M. Fry. 2002. "Jupiter's Cloud Structure as Constrained by Galileo Probe and HST Observations." *Icarus* 157: 373-400.

Sromovsky, L.A., P.M Fry, and K.H. Baines. 2002. "The Unusual Dynamics of Northern Dark Spots on Neptune." *Icarus* 156: 16-36.

Stratman, P.W., A.P. Showman, T.E. Dowling, and L.A. Sromovsky. 2001. "EPIC Simulations of Bright Companions to Neptune's Great Dark Spots." *Icarus* 151: 275-285.

Tollefson, J.W., I. de Pater, P.S. Marcus, S. Luszcz-Cook, L.A. Sromovsky, P.M. Fry, L.N. Fletcher, and M.H. Wong. 2018. "Vertical Wind Shear in Neptune's Upper Atmosphere Explained with a Modified Thermal Wind Equation." *Icarus* 311: 317-339.

van Dokkum, P.G. 2001. "Cosmic-Ray Rejection by Laplacian Edge Detection." *The Publications of the Astronomical Society of the Pacific* 113 (789): 1420-1427.

Wong, M.H. 2022. "Neptune's Dark Vortex NDS-2018." Dataset, *Barbara A. Mikulski Archive for Space Telescopes*. DOI 10.17909/99vs-b998.

Wong, M.H. 2011. "Fringing in the WFC3/UVIS detector." *Proceedings of the 2010 Space Telescope Science Institute Calibration Workshop*. Baltimore, MD: Space Telescope Science Institute.

Wong, M. H., A. A. Simon, J. W. Tollefson, I. de Pater, M. N. Barnett, A. I. Hsu, A. W. Stephens, G. S. Orton, S. W. Fleming, C. Goullaud, W. Januszewski, A. Roman, G. L. Bjoraker, S. K. Atreya, A. Adriani, and L. N. Fletcher. 2020. "High-resolution UV/Optical/IR Imaging of Jupiter in 2016-2019." *The Astrophysical Journal Supplement Series* 247: 58 (25 pp.).

Wong, M. H., J. Tollefson, A. I. Hsu, I. de Pater, A. A. Simon, R. Hueso, A. Sánchez-Lavega, L. Sromovsky, P. Fry, S. Luszcz-Cook, H. Hammel, M. Delcroix, K. de Kleer, G. S. Orton, and C. Baranec. 2018. "A New Dark Vortex on Neptune." *The Astronomical Journal* 155: 117 (9 pp.).

Wong, M. H., M. Ádámkovics, S. Benecchi, G. Bjoraker, J. T. Clarke, I. de Pater, A. R. Hendrix, F. Marchis, M. McGrath, K. Noll, K. A. Rages, K. Retherford, E. H. Smith, and N. J. Strange. 2009. "A Dedicated Space Observatory For Time-domain Solar System Science." *AAS/Division for Planetary Sciences Meeting Abstracts* 41: 16.09

Young, C., M. H. Wong, K. M. Sayanagi, S. Curry, K. L. Jessup, T. Becker, A. Hendrix, N. Chanover, S. Milam, B. J. Holler, G. Holsclaw, J. Peralta, J. Clarke, J. Spencer, M. S. P. Kelley, J. Luhmann, D. MacDonnell, R. J. Vervack, K. Rutherford, L. N. Fletcher, I. de Pater, F. Vilas, L. Feaga, O. Siegmund, J. Bell, G. Delory, J. Pitman, T. Greathouse, E. Wishnow, N. Schneider, R. Lillis, J. Colwell, L. Bowman, R. M. C. Lopes, M. McGrath, F. Marchis, R. Cartwright, and M. J. Poston. 2021. "The science enabled by a dedicated solar system space telescope." *Bulletin of the American Astronomical Society* 53: 232 (8 pp.).

Supplementary material for "Evolution of a Dark Vortex on Neptune with Transient Secondary Features"

Michael H. Wong, Lawrence Sromovsky, Patrick Fry, Agustín Sánchez-Lavega, Ricardo Hueso, Jon Legarreta, Amy A. Simon, Raúl Morales-Juberías, Joshua Tollefson, Imke de Pater, and Patrick G.J. Irwin

Table S1. NDS-2018 and secondary dark feature sizes.

Epoch	NDS-2018		Secondary feature	
	Longitudinal width (deg)	Latitudinal width (deg)	Longitudinal width (deg)	Latitudinal width (deg)
2018.69	26.0 ± 4.5	10.5 ± 2.3		
2018.85	26.0 ± 1.0	9.8 ± 0.5		
2019.74	15.2 ± 0.5	9.4 ± 0.1	20.6 ± 7.0	8.1 ± 8.8
2020.02	15.9 ± 0.3	8.9 ± 0.1	16.9 ± 1.3	8.0 ± 0.5
2020.48	16.1 ± 0.1	9.6 ± 0.1	9.1 ± 0.6	7.7 ± 0.3
2020.63	16.6 ± 0.3	9.7 ± 0.3	12.5 ± 2.6	9.4 ± 1.9
2020.95	16.9 ± 0.2	9.0 ± 0.1		